國立臺灣大學理學院物理學研究所

碩士論文

Department of Physics

College of Science

National Taiwan University

Master Thesis

多焦雙光子體積顯微鏡於果蠅腦之功能性影像

Functional Volumetric Imaging of *Drosophila*

and System Improvement of High-speed

Multifocal Two-photon Microscopy

汪伯元

Po-Yuan Wang

指導教授：朱士維 博士

Advisor: Shi-Wei Chu, Ph.D.

中華民國 111 年 9 月

September, 2022

謝辭

能完成這篇碩士論文，首先我要感謝我的指導教授朱士維老師，在這兩年多來提供許多研究上的建議，不論是光學上的知識或是硬體上的架設，都可以朱老師身上學習到各個方面的學問。朱老師注重口頭報告的邏輯也讓我學習到如何清楚地讓別人理解我的想法，雖然我認為我還有很大的進步空間，但相信比起剛進實驗室的我進步許多。同時我要感謝清華大學的朱麗安教授以及瑞煌提供果蠅樣本，使我們的系統能真正的應用在果蠅身上。

再來我要感謝實驗室的學長姐們，首先是帶我了解這套高速系統的宇軒，感謝你在我剛加入實驗室的時候不厭其煩地教導我很多系統上的光學元件以及硬體架設，即是畢業後很有耐心的解答我的疑問。建昇，很謝謝你細心的教導我MATLAB 的語法，讓我能修改你的程式來跑我們取得的生物影像。冠傑，感謝你經常花時間跟我們討論研究的方向，也抽空來聽我的口試彩排並提供了許多有用的建議，祝福你順利完成你的博班學位。邦漢，謝謝你提供了很多未來人生中實用的建議。鴻羽，很謝謝你能在我做實驗的時候幫我開果蠅腦，大幅增加了做實驗的速度，雖然你很瘋狂，常常講一些不正經的話，但也因此讓做實驗的過程更加有趣。俊誼，感謝你解答很多光學以及神經相關的問題，也在分析上提供很多很有幫助的建議，看你跟鴻羽在七樓一搭一唱真的帶給我們很多歡笑。

接下來是實驗室的同儕，首先是德心，很謝謝你在我的論文寫作上提供了很多建議，讓我的文章看起來通順許多。采穎，感謝你在果蠅分析上提供了很多重要的建議，很開心能跟你一起打球，也祝福你未來能順利的取得果蠅樣本。敏翔，雖然你一天到晚都在我的位子上丟垃圾，不過最後有請我吃壽司吃到飽，我想應該可以一筆勾銷。庭禎，很感謝你在系統的軟體上面做了很多修正以及測試，讓我們可以更快的解決系統上的問題。展麟、重名、荇軒、柏學、尹慈、Kentaro，很開心能跟你們在一起實驗室聊天以及解決各種大大小小的問題。

這裡我也要謝謝芷菱以及我的朋友們，在我心情低落時傾聽並且陪伴著我，給我心靈上的很大的支持。最後，我要感謝我的家人們，感謝你們能讓我在就讀碩班的過程中無後顧之憂，並且支持我所做的決定，讓我能順利的完成我的碩士論文。

i

摘要

為了了解大腦的機制，腦神經影像技術在一個多世紀以來經歷了許多突破性的發展，然而我們對大腦的了解依然有限。迄今為止仍然沒有理想的影像技術能夠同時在整個大腦中實現足夠高的時空間解析度。為了達成這項目標，此研究裡我們以果蠅作為我們的模式生物，因為其極小的大腦體積，且具有相對完整的神經結構性圖譜。為了取得活體果蠅全腦功能性影像，我們需要達到以下需求：（Ⅰ）非侵入性觀測；（Ⅱ）微米尺度的空間解析度以分辨單一神經元；（Ⅲ）～一百微米的穿透深度以進行果蠅腦中的深組織影像；（Ⅳ）毫秒等級時間解析度的體積影像以觀察三維空間中的功能性影像。

由於雙光子光學顯微鏡的眾多優點，其經常被用於大腦功能性研究，例如其非侵入性及微米尺度的空間解析度，光學切片能力亦適合進行深組織影像，達成了需求（Ⅰ～Ⅲ）。然而，大部分雙光子顯微鏡透過掃描整個樣本以獲得三維影像，限制了其影像速度。在此研究中我們分別在橫向及軸向加快成像速度以達成高速三維影像。在橫向上，我們利用繞射分光元件將單道光分成 32 道光，並使用 32 通道的光電倍增管提高其影像速度。在軸向上，我們使用可調式聲波梯度折射率透鏡達成焦點在此軸上的高速掃描。透過這結合這兩項技術，我們實現了時間解析度為兩毫秒的體積影像，即達成需求（Ⅳ）。

此研究使用鈣離子螢光蛋白（GCaMP7f）標記的果蠅腦進行活體觀測，透過觀察自發活動，發現了果蠅腦內蕈狀體中不同亞區的瞬時反應。通過進一步以電擊刺激果蠅，我們在頻域中觀察到週期性活動。證明了此系統能夠觀察活體果蠅腦的功能性影像。然而，在我們系統中還有一個需要被解決的問題：資料擷取過程中的數據遺失。可能的原因為軟體的過度負載，造成中央處理器的低處理效率。在未來更換較高效能的中央處理器後，期望我們所建立的高速多焦點多光子體積顯微鏡，能夠對於未來建立果蠅大腦的功能性神經連接圖譜有所幫助。

關鍵字：多焦點顯微鏡、雙光子顯微鏡、可調式聲波梯度折射率透鏡、體積成像、功能性影像

ABSTRACT
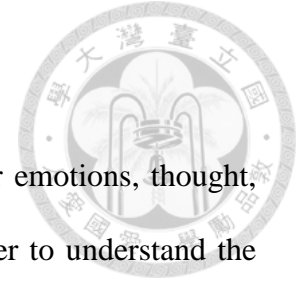
Brain is an important organ that plays a necessary role in our emotions, thought, memory, and almost every process that regulates our body. In order to understand the mechanism of the brain, numerous studies have progressed for more than a century. However, our understanding of the brain is still limited. The reason is that no ideal imaging tool nowadays has the capability to simultaneously achieve micrometer and millisecond spatiotemporal resolution in the whole brain. To achieve this requirement, we select *Drosophila* to be our sample because of its small brain size and the nearly-complete structural connectome. In order to accomplish *in vivo* whole *Drosophila* brain functional imaging, we need to reach the following requirements: (I) noninvasive method, (II) micrometer spatial resolution to distinguish neurons, (III) ~100 μm penetration depth for *Drosophila* deep tissue imaging, (IV) millisecond temporal resolution volumetric imaging for 3D functional dynamics.

Two-photon microscopy (2PM) is often used for *in vivo* brain study because of its noninvasive characteristic, ~μm scale spatial resolution and optical sectioning that offers remarkable penetration depth, achieving the requirements (I - III), respectively. However, the imaging speed is limited since 2PM typically requires raster scanning through the whole sample. Here we increase the speed on the lateral axis via multifocal imaging formed by a diffractive optical element (DOE) and a multichannel PMT. The axial speed is enhanced by a tunable acoustic gradient-index (TAG) lens, which scans the focus on the axial axis with an ~100 kHz. Through combining these two optical elements, we are able to achieve volumetric imaging with ~2 ms temporal resolution, which accomplishes the last requirement (IV).

In this study, we apply our system on the GCaMP7f-labeled *Drosophila* brains for *in vivo* imaging. With spontaneous activities, we discover the distinct transient response

in different subcompartments in the mushroom body. We further stimulate the *Drosophila* via electric shock, and observe periodic activities in the frequency domain. However, one challenge remains is the data lost during imaging, which is caused by the software-induced low CPU processing efficiency. With replacing a high-performance CPU to overcome this difficulty in the future, our high-speed multifocal multiphoton volumetric microscope paves the way toward establishing functional connectome in *Drosophila* brain.

CONTENTS

LIST OF FIGURE

LIST OF TABLE

Chapter 1. Introduction: Challenges of brain study and possible solutions

Brain is an important and complex organ composed of astronomical numbers of neurons that plays a necessary role in our emotions, thought, memory, and almost every process that regulates our body. However, despite numerous studies that have progressed for more than a century, our knowledge about brain function is still limited, due to the lack of proper tools that achieve high-speed volumetric image and sub-cellular resolution simultaneously for large scale brain imaging. Thus, in this study, we increase the imaging speed to achieve high-speed volumetric two-photon microscopy and apply our system for *in vivo* functional brain study.

1.1 Current status in brain study

Brain study is one of the most important domains in science. "What is the biological basis of consciousness?" and "How are memories stored and retrieved?" are in the top 25 questions recorded in the 125-anniversary special section of *Science* [1]. The following chapter will introduce some basic brain features and current state-of-the-art brain imaging techniques.

1.1.1 Brain features

The brain controls our senses, high-order function and is also related to some common diseases such as depression. To reveal how the brain works and how it affects our daily behavior, studying the building component of the brain structure is necessary. The basic component of the brain, which is neuron, has been debated between Golgi and Cajal in

the 19th century [2]. Followed by the studies of more than 100 years by biologists and neurologists, the features of a single neuron are well-known. Fig. 1.1.1a is a single neuron, commonly constructed by a soma (i.e. cell body) and neurites. Soma houses the nucleus and offers cellular activities to keep the neuron functional. Neurites are responsible for collecting and transmitting signals, and they are classified into dendrites and axons. Dendrites receive the incoming signals from nearby neurons and send them to the cell body. The length of dendrites are rarely longer than 2 mm. Axons, on the other hand, extend a meter or more inside our body and transmit signals from the cell body to the axon terminal [3]. The signals transport between the neurons are known as action potential, which is controlled by the membrane potential of a neuron. The ions passing through the membrane causing the action potential (i.e. electrical pulse) promptly rises and falls with a time span of ~2 ms, as shown in Fig. 1.1.1b.
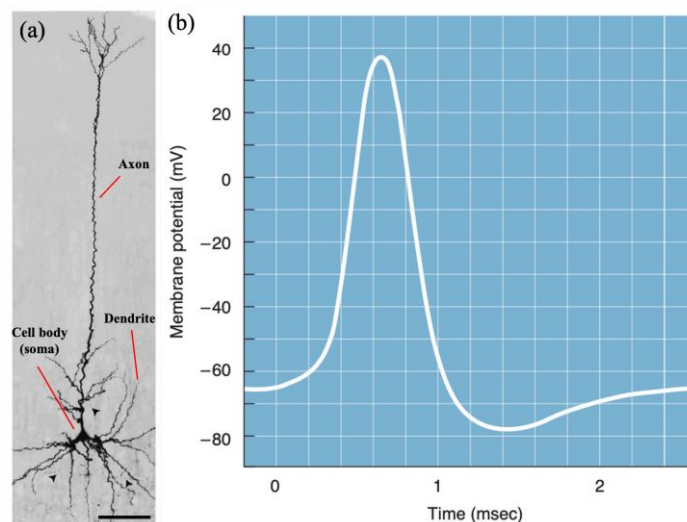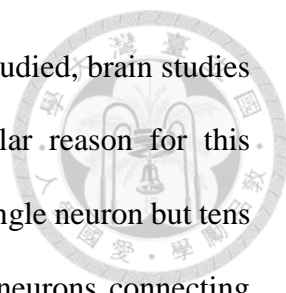
Fig. 1.1.1 Neural structure and action potential

(a) Extended-focus views of rat pyramidal cells stained for biocytin [4]. Scale bar, 50

μm. (b) An action potential recorded by electrophysiology and oscilloscope [3].

2

However, even though the characteristic of a single neuron is well-studied, brain studies still challenge scientists and neurologists nowadays. The particular reason for this circumstance is that the function of the brain is not carried out by a single neuron but tens of thousands of neurons with multiple upstream and downstream neurons connecting together, also called "connectome". Taking olfactory information in a *Drosophila* brain, for example, it arrives at the antenna lobe (AL) primarily via antennal nerve (AN). The signals then pass through the projection neuron (PNs) and are received by the dendrites of the Kenyon cells (KC), also known as calyx (Ca) (Fig. 1.1.2a). The Kenyon cells are famous for forming the mushroom body (MB), a brain region which plays an important role in olfactory learning and memory in insects. As shown in Fig. 1.1.2b, the input of MB is not only olfactory signals, but also information such as visual and temperature [5]. Since the numerous neurons that interact with the MB introduced above are already complicated, not to mention the neurons in the whole brain intricately communicate with each other, thus forming a complex connectome and giving rise to the emergent property of the brain. Therefore, a microscopy that covers more regions of the brain, furthermore with high spatiotemporal resolution, benefits to reveal the mystery of the brain [6]. In the next section, common techniques and challenges in brain research are introduced.
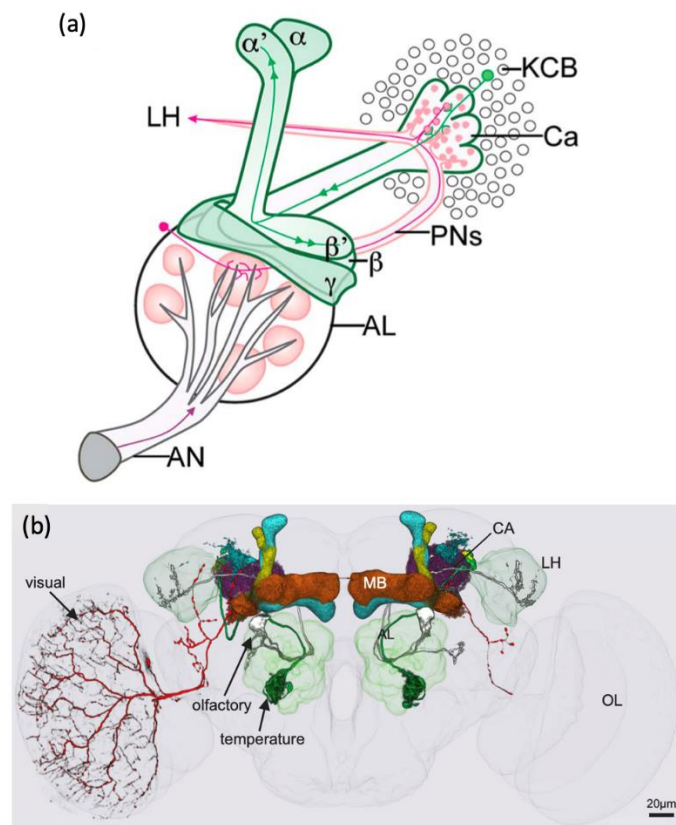
Fig. 1.1.2 Connectome of *Drosophila* mushroom body

(a) Olfactory pathway of the *Drosophila* right brain from anterior aspect [7].

(b) Sensory information input of MB [5].

1.1.2 Challenges of common technique in brain science

To make a brief sum up of the technology required in brain science, an ideal observation tool needs to have a micrometer scale spatial resolution to resolve different neurons, whose cell bodies range from 2 μm to 20 μm, depending on different species [8]. Beside spatial resolution, millisecond scale temporal resolution is necessary to observe the action potential or the rising time of a genetically encoded indicator to distinguish the time sequence from different neurons. Last but not least, a large enough imaging area is preferable since it covers as many brain neurons as possible; in other words, a whole brain study is the ultimate goal. However, notice that there is a tradeoff here, by maintaining the same spatial resolution to see every single neuron and dwell time of every pixel,

4

increasing the imaging area causes the growth of the pixel number, resulting in lower temporal resolution.
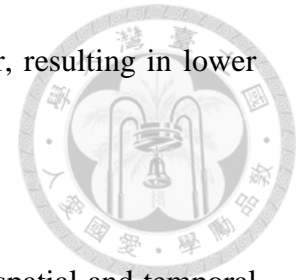
Overall speaking, it is difficult to observe a whole brain with high spatial and temporal resolution simultaneously. For example, functional magnetic resonance imaging (fMRI), a well-known technique which achieves whole human brain imaging with ~ 10 ms temporal resolution [9], but with a poor spatial resolution with only few millimeters [10], is not able to distinguish a single neuron and is much more suitable to observe different brain regions [11] (Fig. 1.1.2a). Electrophysiology, on the other hand, utilizing micro-electrodes simply measures the electrical signal of the neuron directly, thus having excellent micrometer spatial resolution and sub-microsecond temporal resolution. However, the number of micro-electrodes is limited since it will interfere with the brain function [12, 13], so this technique also cannot achieve observing every single neuron in whole brain study (Fig. 1.1.2b). However, optical microscopy manipulates light to excite or illuminate the neurons and receive the photons by detectors for image information, offering a sub-micrometer spatial resolution and millisecond scale temporal resolution [14]. Although it has sufficient high spatiotemporal resolution, it suffers from a relatively small region of interest (~ mm^3) [15], which is not large enough to cover the whole human brain (Fig. 1.1.2c, d). Even though the human brain is our ultimate aim of functional brain study, the large size is not suitable for whole brain high-speed imaging with optical microscopy [16]. One way to achieve this whole brain study is to utilize small model animals, for example *Drosophila*.
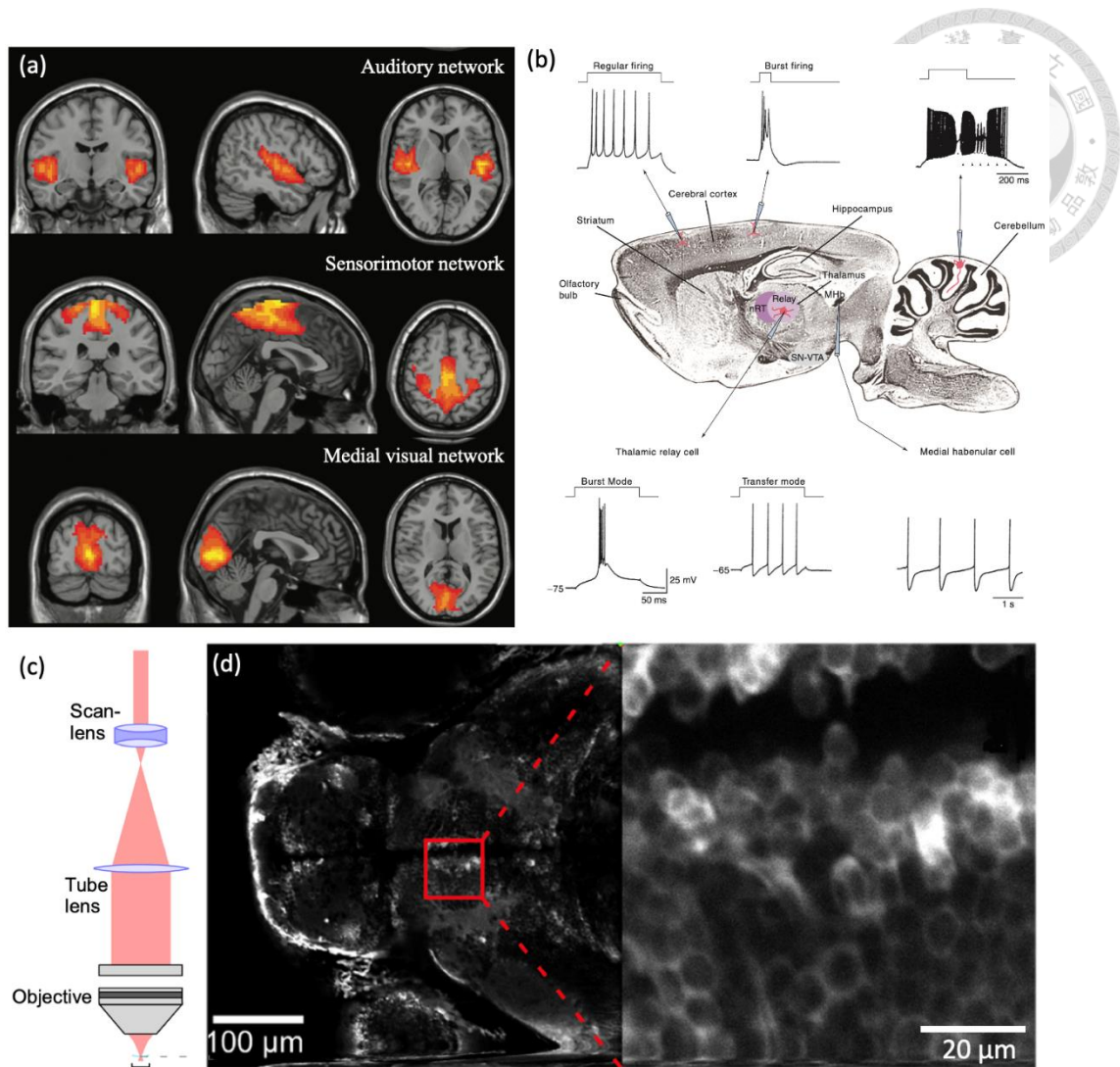
Fig. 1.1.3 Common techniques in brain study

(a) Several typically reported neurons with active regions of the human brain shown in orange color (adapted from [17]), although fMRI is able to observe clear macroscopic structure, it lacks the ability to observe a single neuron. (b) Neuron signals in the mammalian brain display varying electrophysiological properties [18]. (c) Schematic of laser scanning optical microscopy [19]. (d) *In vivo* larval zebrafish labeled with GCaMP6f observed by two-photon microscopy, the individual somata is seen in the right figure (Figure adapted from [19]).

6

1.1.3   Model animal: *Drosophila*

The model animal we used is *Drosophila Melanogaster*, also known as fruit fly. Compared to human and other model animals such as mice, the size of the *Drosophila* brain is way smaller and whole brain study is more practical, as shown in figure 1.1.4. Even though it has a minuscule brain size (~ 200 μm × 750 μm × 360 μm), it has about 1.3×10^5 brain neurons [8] to form a complex enough behavior and connectome map (Table 1.1.1). Throughout 100 years of biologist studies, a nearly-complete structural connectome has been established [20-22], which acts as a crucial reference for establishing *in vivo* functional connectome. Furthermore, nearly 75% of human disease-causing genes have homolog in *Drosophila* [23], such as Alzheimer's and Parkinson's disease, making it one of the most important model animals among neurological studies and the "first draft" model before human whole brain studies [24].
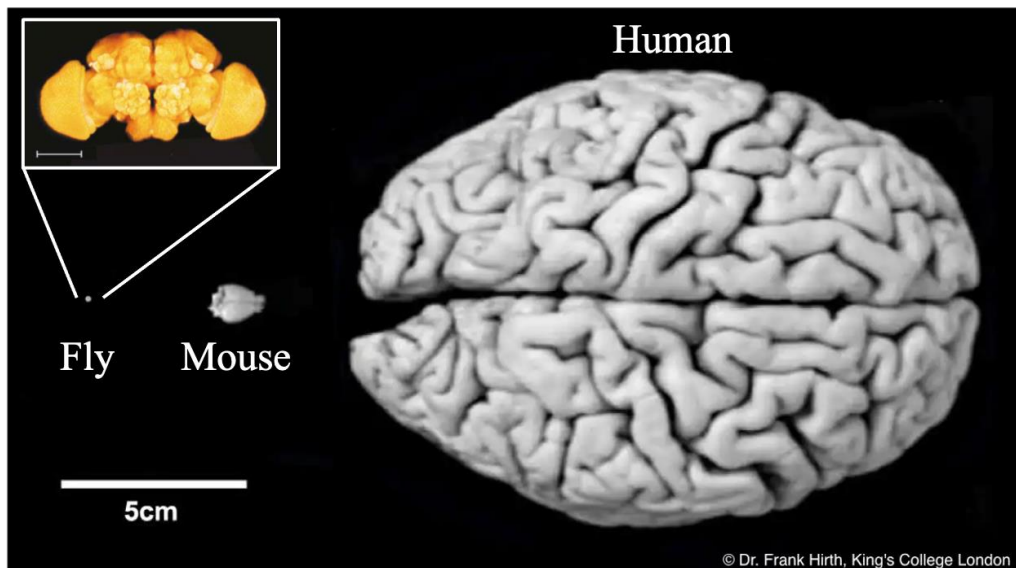
Fig. 1.1.4 Comparison of brain volume between human, mouse and *Drosophila*

The scale bar of the inset image is 100 μm. [25] (Figure adapted from https://the conversation.com/ode-to-the-fruit-fly-tiny-lab-subject-crucial-to-basic-research-38465)

	Human	Mouse	*Drosophila*
Brain volume	1.6×10^6 mm^3	440 mm^3	8×10^{-2} mm^3
Number of brain neurons	8.6×10^{10}	7.1×10^7	1.3×10^5

Table 1.1.1 Parameter of brain features in human, mouse and *Drosophila*. [8, 16]

1.1.4 Challenges of *in vivo Drosophila* brain study

To achieve *in vivo* whole brain imaging with optical microscopy in *Drosophila*, some fundamental challenges need to be overcome. First, to match up the animal behaviors and the brain neuron activities, a noninvasive method for *in vivo* study is required to reduce damage on living organisms. Second, the size of the soma in the *Drosophila* brain is about 6 μm [26], so micrometer scale spatial resolution microscopy is necessary to distinguish neurons. Third, to reach the deep tissue area, hundreds of micrometer penetration depth is needed. Fourth, the neuron distribution in the *Drosophila* brain, like in any other animal, is three dimensional, so a volumetric microscopy tool is highly desirable. Last but not least, to capture the action potential or the rising edge of ion dynamics, millisecond scale temporal resolution microscopy is necessary for functional brain imaging (Table 1.1.2). Despite the fact that each requirement can be achieved individually, in order to achieve *in vivo Drosophila* whole brain imaging with high spatio-temporal resolution, these conditions should be accomplished simultaneously, and no microscope is able to complete these requirements until now [27].

Drosophila brain characteristic	Requirement
in vivo brain study	Noninvasive method
~ 6 μm neuron size	Spatial resolution: micrometer scale
Deep tissue	Penetration depth: hundreds of micrometers
3D structure	Volumetric imaging
~2ms action potential	Temporal resolution: millisecond scale

Table 1.1.2 Requirements for *in vivo Drosophila* brain study.

1.2 Comparison of brain study techniques

Great technique brings out great experimental data, which improves the edge of science. As Robert A. Millikan mentioned when he received the Nobel Prize in 1923 [28],
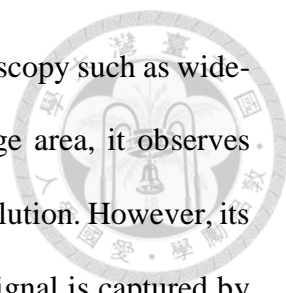
The fact that Science walks forward on two feet, namely theory and experiment. ... Sometimes it is one foot which is put forward first, sometimes the other, but continuous progress is only made by the use of both by theorizing and then testing, or by finding new relations in the process of experimenting and then bringing the theoretical foot up and pushing it on beyond, and so on in unending alterations.

In this following section, suitable tools will be chosen to form a combination for high-speed and whole brain study in *Drosophila*.

1.2.1 Optical microscopy in brain imaging

As mentioned above, optical microscopy with small animal models seems to be the leading solution for probing the functional connectome in brains. Not only is optical microscopy noninvasive, but it also offers sub-micrometer spatial resolution, which accomplishes two out of five of our requirements. One of the problems left is deep tissue

observation, i.e. large penetration depth. For traditional optical microscopy such as wide-field imaging based on camera (Fig. 1.2.1a), by illuminating a large area, it observes multiple neurons simultaneously and provides remarkable digital resolution. However, its disadvantage is crosstalk due to tissue scattering, which means the signal is captured by nearby pixels. While it illuminates and detects signals from the whole volume, wide-field imaging lacks the ability of optical sectioning. With these two cons above, contrast decreases in all three axes, making signal intensity severely lower in deep-tissue imaging. Penetration depth of wide-field imaging is typically limited to less than 100 μm [29], so it is more suitable for thin samples and not for our purpose [15, 30].

Confocal microscopy (Fig. 1.2.1b), on the other hand, avoids both lateral and axial low contrast that occur in observation. The lateral scattering effect decreases due to the use of single-channel detector and single-beam raster scanning, thus avoiding crosstalk. The signals are gained in a time sequence and then assembled into one or multiple images. In order to increase the axial contrast, a pinhole is used to block the out-of-focus signals, thus only capturing the signals around the focus, which is also known as optical sectioning [31]. These advantages on increasing the contrast are more suitable for deep tissue imaging [32].

Two-photon microscopy (2PM) also offers optical sectioning (Fig. 1.2.1c), since two photon effects only occur around the focal point [33]. Absorption and fluorescence no longer happens at the out-of-focus area, thus decreasing photobleaching and phototoxicity effects compared to confocal microscopy [34]. With 2PM based on near infrared excitation wavelengths for excitation, it reduces the scattering effects when light passes

10

through the tissue, resulting in longer penetration depth to millimeters [35, 36]. Thus, we select two-photon laser scanning microscopy to be our imaging technique in this study.
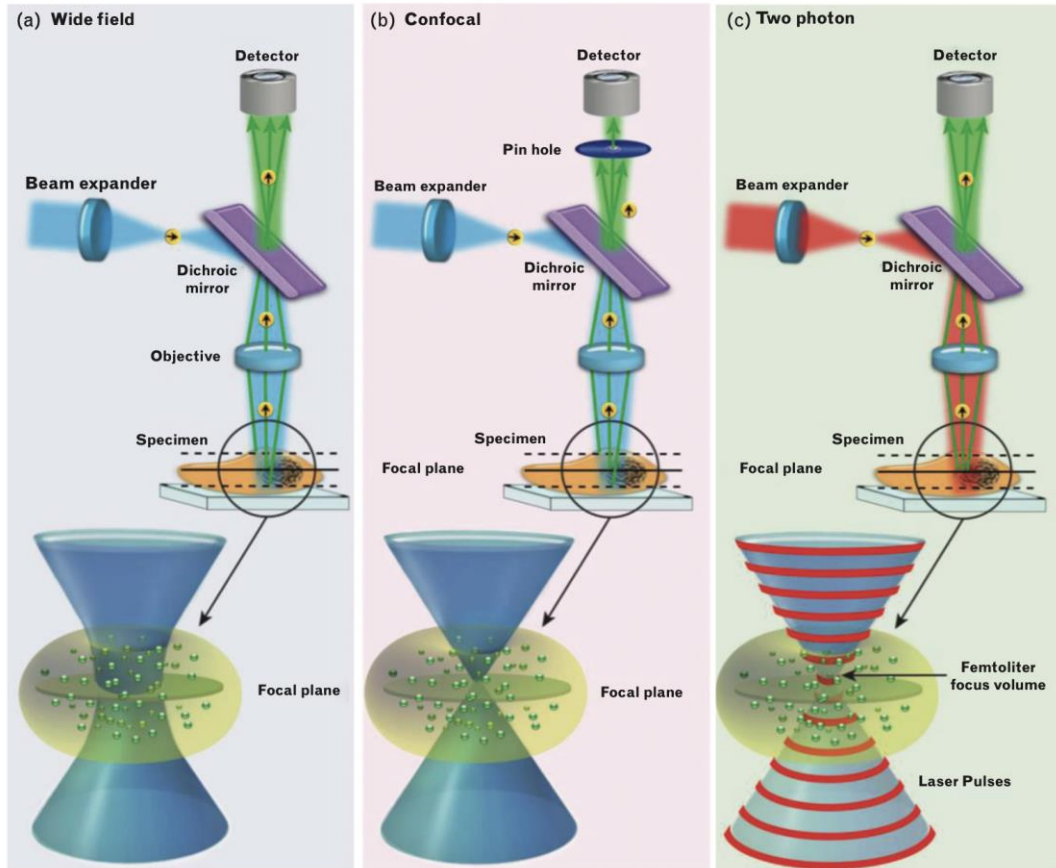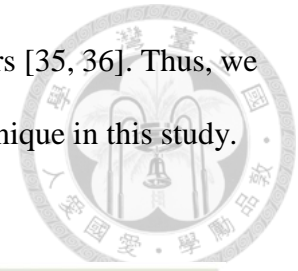
Fig. 1.2.1 The schematic between wide-field, confocal and two-photon microscopy (a) Wide-field microscopy: Light illuminates the whole volume through the light path and detects every signal from the sample. (b) Confocal microscopy: Light also illuminates the whole volume but only detects the signals at the focus, while the out-of-focus signals are filtered out by a pinhole arranged in front of the detection. (c) Two-photon microscopy: Laser pulse only illuminates the focal region; thus, the pinhole is no longer needed. 2PM is capable of detecting the signals from the focus. [35]

1.2.2 Speed limitation in two-photon microscopy

2PM's multiple advantages satisfy most of our requirements, including long penetration depth that covers the whole *Drosophila* brain. However, the data acquisition speed of laser scanning microscopy is its major bottleneck, due to the laser focus moving in the sample voxel by voxel. This decreases temporal resolution, which is one of the necessary requirements for observing functional images [37]. Multiple techniques have been invented to solve this speed issue, for example, resonant mirrors [38] and polygonal mirrors [39] have been utilized, which enhance the lateral scanning speed to 100 frames per second [40]. With the use of a single-channel detector, the data acquisition rate is restricted to ~500 MHz because of the fluorescence lifetime, which is about 2-3 ns. Thus, intuitively utilizing a multichannel detector with multifocus drastically increases the data throughput.

1.2.3 Enhancing speed in lateral axis with multifocus (DOE)

Multifocal multiphoton microscopy (MMM), also known as spatially multiplexing multiphoton microscopy, enhances the imaging speed proportionally with the number of foci since parallel multibeam are capable of scanning the region simultaneously. There are several ways to split a single bean into multiple beams, such as microlens arrays, spatial light modulator (SLM) and diffractive optical element (DOE).

Microlens arrays were the earliest version of MMM, which was invented around the 2000s and already has the ability for video-rate imaging [41, 42]. However, when the incident laser beam passes through the microlens, the spaces between the microlens causes energy loss, thus decreasing the transmission rate. Additionally, the intensity

12

distribution of the incident laser is nonuniform, mostly Gaussian beam, resulting in the power difference at the central and the peripheral part.
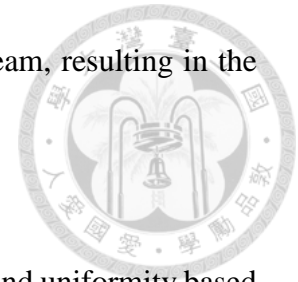
Compared to microlens arrays, SLM offers higher transmission rate and uniformity based on that the liquid crystal arrays are finely adjusted [43]. These computer-controlled liquid crystals inside SLM are in charge of changing the wavefront of the laser and conveniently create arbitrary light patterns, including multifocal. However, the disadvantage of the liquid crystal device is that it is sensitive to high power. Since we utilize high-power femtosecond pulsed laser for two-photon imaging, SLM is also not suitable [44].

DOE, on the other hand, accepts high-power incident laser beam and reaches ~99% transmission rate. It utilizes an imprinted microstructure pattern which changes the phase of the laser passing through it, forming almost any beam shape [45]. Although the disadvantage is that the beam shape is fixed, since it is decided by the microstructure [46]; it is simple to integrate in an optical path, thus we alternatively switch between single-beam scanning and multibeam scanning, forming two techniques into one system. With these advantages mentioned above, DOE seems to be the most suitable tool for forming multifocus. Yet this 2D imaging is not enough, since the *Drosophila* brain is a 3D structure, a volumetric imaging is necessary. To form a high-speed volumetric imaging, we need a proper axial scanning technique while achieving millisecond scale temporal resolution. In the next section, multiple axial scanning techniques will be introduced.

1.2.4 Enhancing speed in axial axis with a TAG lens

In one lateral axis, we have chosen a scanless technique. For the axial axis, there are also several techniques that offer scanless ability which highly increase imaging speed, such

13

as Bessel beam microscopy [47] and light bead microscopy (LBM) [48]. Bessel beam microscopy utilizes optical elements, such as axicon, to elongate the depth of field (DOF) to ~100 μm, which is about 15 times larger than traditional gaussian beam (Fig. 1.2.2a). This needle-shaped intensity distribution on the z axis enables Bessel beam microscopy to avoid scanning along the axial direction, thus enhancing the volume rate [49]. However, since Bessel beam projects 3D information on a 2D image, i.e. lacks optical sectioning ability, it is more suitable for sparse neuron distribution.

LBM, on the other hand, is a variant of Bessel beam that offers optical sectioning ability. Via a series of mirrors and a dichroic, multiple focus is generated along the z axis with time difference between each bead, thus it is able to distribute the signals from different depths (Fig. 1.2.2b). However, since we have already chosen multifocus on the lateral axis, adding a multifocus technique on the axial axis causes numerous foci. This results in the low intensity of each focus, thus the photons collected by the detector will decrease, which is not suitable for high-speed microscopy. Since the above z-scanless techniques are not proper, we introduce several axial scanning techniques below.
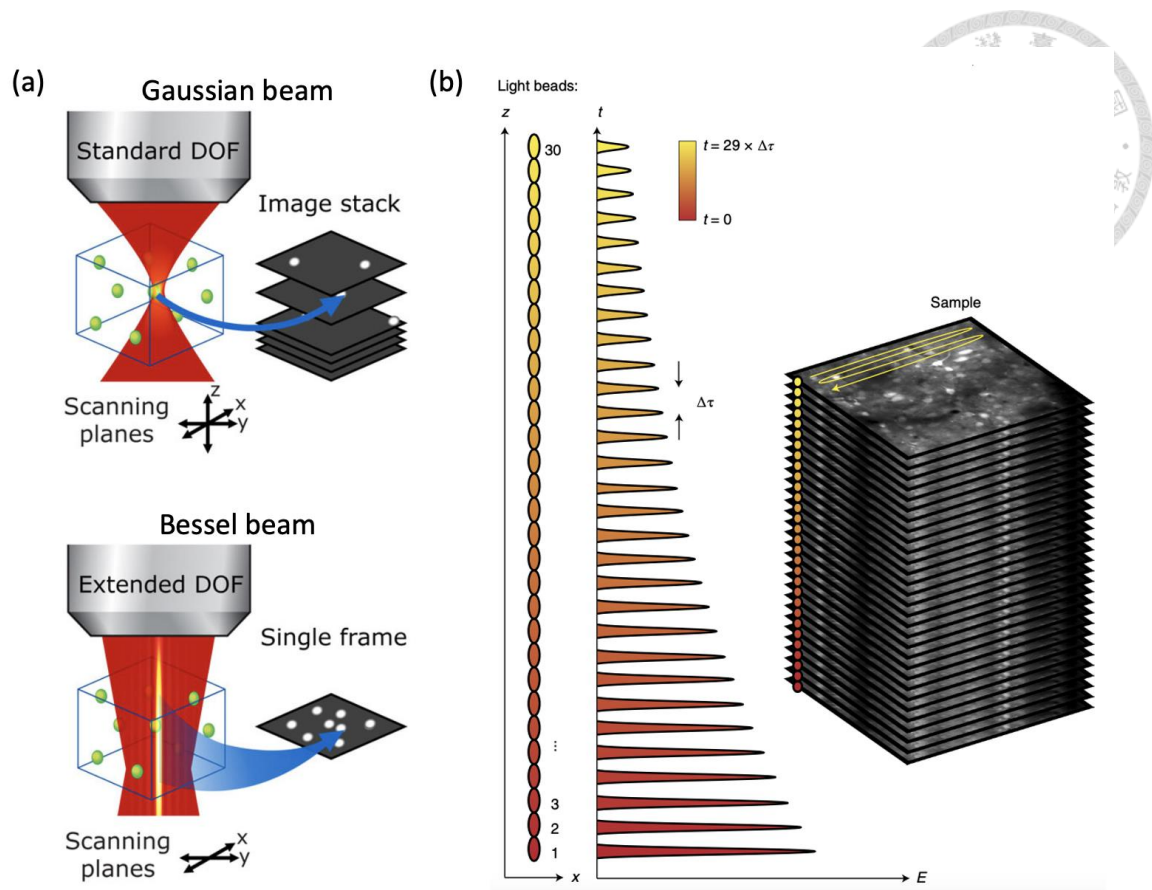
Fig. 1.2.2 The schematic of axial scanless techniques

(a) The comparison between the Gaussian beam and the Bessel beam. Traditional 2PM utilizes a Gaussian beam for 3D scanning, forming an image stack. Bessel beam, on the other hand, extended DOF, which enables the scanless on z axis, but squeezes the volume information into a single frame [50]. (b) LBM generates multiple foci on the axial axis with temporal multiplexing to achieve z axis information [48].

For scanning technique, the most straightforward way to form a volumetric image is to move the objective by a piezoelectric actuator (Fig. 1.2.3a), but the frequency is limited to ~100 Hz due to the inertia of the objective [51], which is not fast enough to achieve high temporal resolution. Compared to the piezoelectric stage, electrically tunable lens (ETL) (Fig. 1.2.3b) has less inertia. ETL utilizes mechanisms such as polymer membrane or electrowetting that allows the axial scanning speed to achieve nearly 1 kHz [15, 52].

15

Multiplane volumetric image has been demonstrated recently with volume rate at 10 Hz [53, 54]. However, the speed is still not fast enough to accomplish a millisecond scale microscopy.
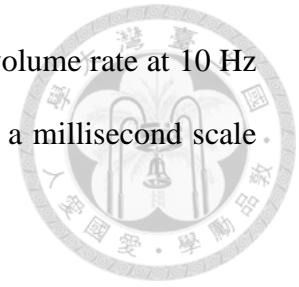
To achieve high-speed axial scanning, inertia-free techniques such as tunable acoustic gradient-index (TAG) lens (Fig. 1.2.3c) offers frequency over 100 kHz [55, 56], which is at least two and three orders faster than ETL and piezoelectric actuator, respectively. With the acoustic wave driving the liquid inside the TAG lens resonantly, the density of the liquid and refractive index changes sinusoidally. Thus, periodically converge and diverge the beam, then by combining TAG lens and objective, they are considered as switching between concave and convex lens. Consequently, from the literature review above, TAG lens has the fastest axial-scanning speed to achieve our millisecond scale microscope, which seems to be the most suitable technique. After combining two-photon, DOE and the TAG lens, we achieve the five requirements which are mentioned at section 1.1.4. This leads to our aim: observing functional images in the *Drosophila* brain with our high-speed MMM.
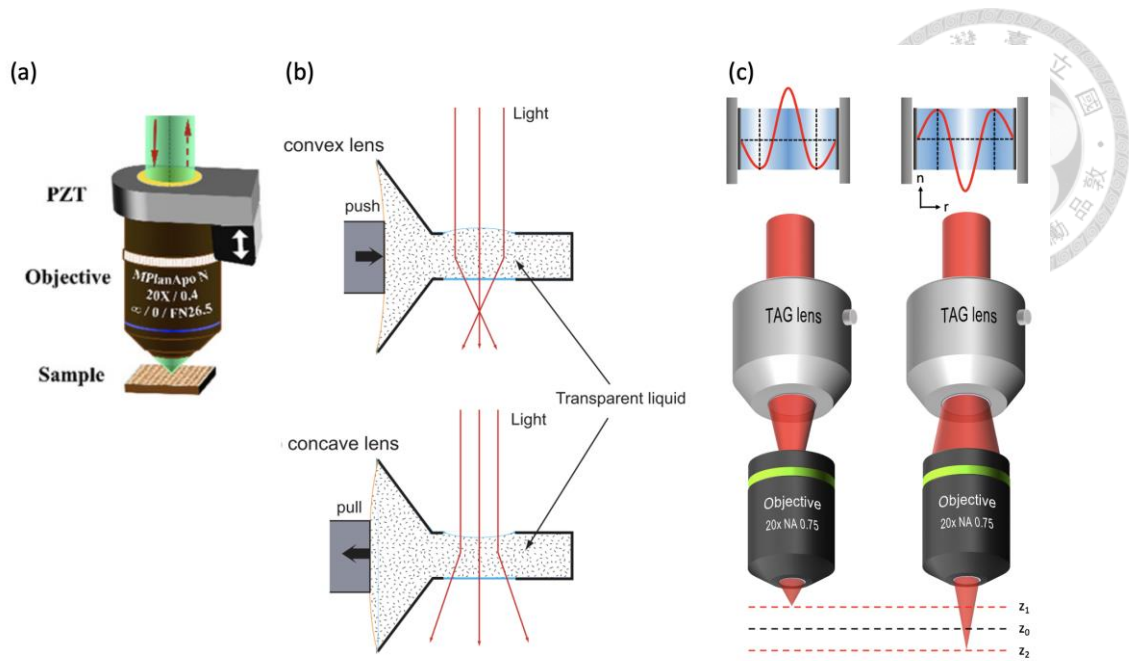
Fig. 1.2.3 The schematic of axial scanning techniques

(a) Piezoelectric actuator mounted on the objective to generate a z axis scanning.

(Figure adapted from [57].) (b) ETL is driven by electricity, take liquid lens for

example, by pushing and pulling the orange membrane on the left, the transparent liquid

inside the lens will cause the shape changes on the blue membrane, thus bending the

light passing through [58]. (c) TAG lens is an acousto-optics element, the refractive

index of the liquid changes by acoustic wave, thus converges and diverges the laser

beam, forming a high-speed axial scanning technique. (Image courtesy: Y.-H. Tsai)

1.3 Aim: Functional volumetric brain imaging in *Drosophila* brain study

In summary, for the purpose of observing the *in vivo* functional imaging in *Drosophila*

brain, we utilize a two-photon volumetric millisecond-scale multifocal microscope.

Multifoci are generated on the lateral axis by DOE, this scanless technique on one lateral

axis highly increases the imaging speed proportionally with the number of foci. The TAG

lens scans the axial axis with an extremely high frequency. With the combination of DOE,

17

TAG lens and 1D galvanometric mirror, a volumetric image is completed; and via DOE and TAG increasing the imaging speed on two axes, millisecond scale temporal resolution is also achieved. Other requirements such as non-invasive method, micrometer scale spatial resolution and high penetration depth are provided since the two-photon optical microscopy inherently offers. In this study, we not only observe functional activity by this high-speed MMM, but also enhance the performance of this system. In the next chapter, we will introduce the principle of each technique in our system we have chosen.
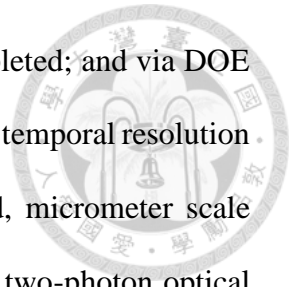
Chapter 2. Principle of each technique

In this chapter, we will describe the principle of the mechanism we have chosen, including two-photon microscopy, DOE and TAG lens. The combination of these above techniques which achieve a volumetric imaging will also be explained.

2.1 Two-photon microscopy

Our high-speed microscope is based on two-photon excitation. The theory was presented in 1931 by Maria Göppert-Mayer [59]. Compared to single-photon excitation, two-photon excitation is when an electron of a molecule absorbs two identical energy photons simultaneously and is excited to the excited state from the ground state. The electron will then decay back to the ground state and emit a fluorescence photon (Fig. 2.1.1).
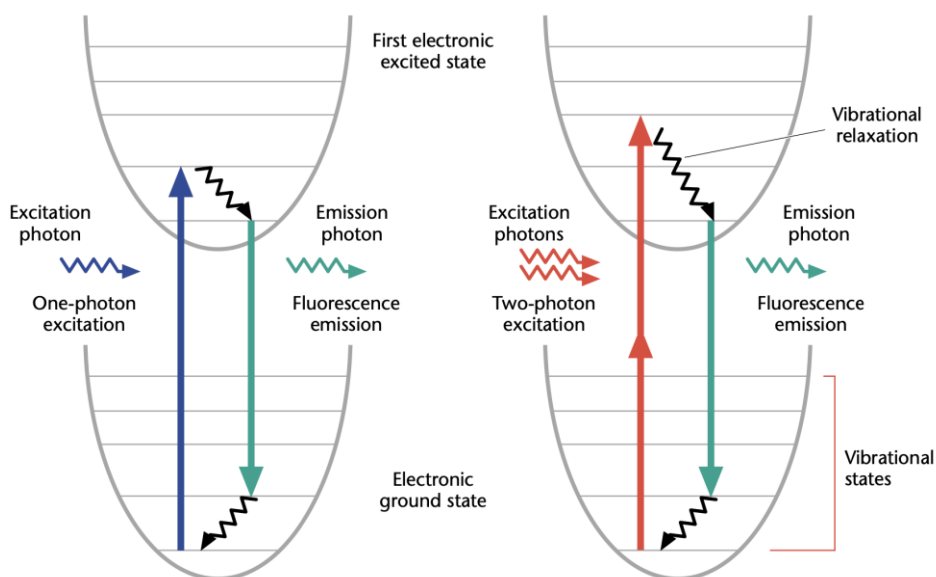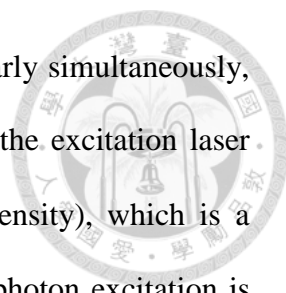

Fig. 2.1.1 Jablonski diagram of single-photon and two-photon excitation

The fluorophores that absorb single and two photons are excited to the first electronic

states from the ground state [60].

Since the two-photon excitation requires absorbing two photons nearly simultaneously, the probability of this effect is lower, it depends quadratically on the excitation laser intensity ($S \propto I^2$, S: absorption probability, I: excitation laser intensity), which is a nonlinear effect [61]. On the other hand, the probability of single-photon excitation is simply proportional to the excitation laser intensity. As shown in Fig. 2.1.2, the excitation linearly occurs at all cone volume at single-photon excitation while only the focal area is excited at two-photon excitation. The unit Göppert-Mayer (GM), named in her honor, is used to quantify the molecular two-photon absorption cross-section, which defines the absorption probability. However, the range of the common fluorescence dye is 1-300 GM [61], where one GM is 10^{-58} m^4s/photon, thus extremely low probability occurs at two-photon excitation. To solve this problem in 2PM, an ultra-short pulsed laser with ~100 fs pulse width is often utilized to concentrate the photons into discrete pulses [34]. Since the photons are confined in the temporal region with pulse laser, 2PM also converges the photons at the spatial region with an objective, which is $\sim \mu m^2$ size. These two confinements in both spatio-temporal regions highly enhance the probability of two photons arriving at the fluorophore at the same time while still maintaining the average power relatively lower than the sample tolerance limit [14].

With these difficult requirements, give rise to two significant advantages in 2PM. First, since the electron absorbs two photons simultaneously, the energy of the photons will be approximately half less compared to single-photon excitation. This means longer wavelengths are used for excitation, mostly near infrared region, due to the less affected by tissue scattering, this leads to longer penetration depth [62]. Second, the nonlinearity of two-photon excitation leads to the excitation only happening at the focal area. As shown in Fig. 2.1.2, this provides optical sectioning ability in volumetric imaging, thus

20

resulting in enhancing the imaging contrast [14]. Since the focal plane is excited, this advantage in decreasing the photobleaching and phototoxicity effects, which is more suitable for living samples [34].
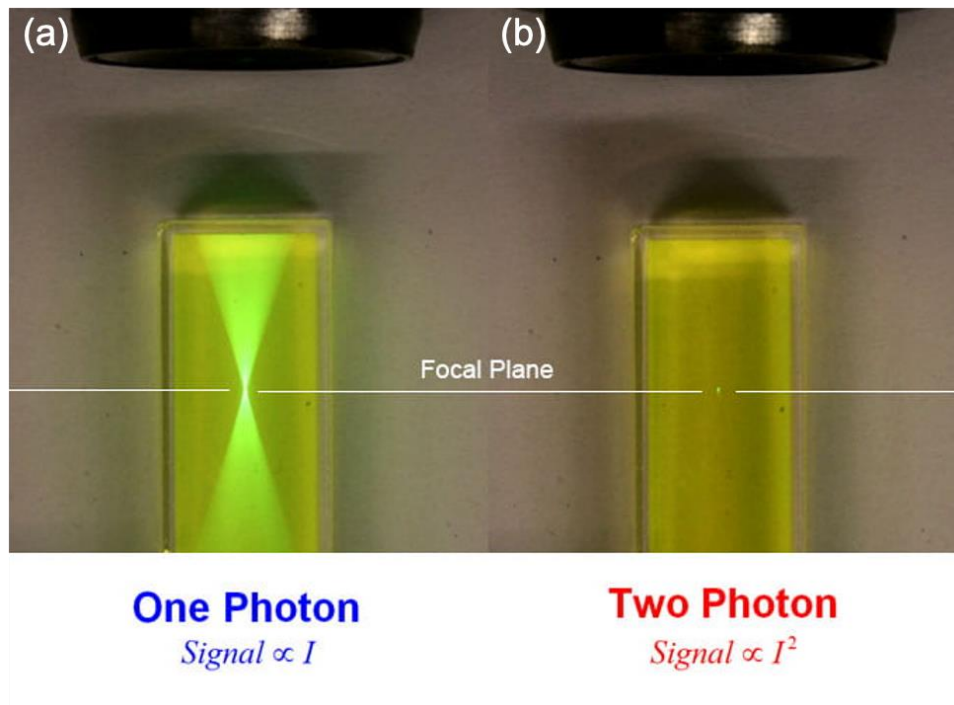
Fig. 2.1.2 Fluorescence excitation in single-photon and two-photon microscopy

(a) Fluorescence occurs along the light cone in single-photon excitation due to the signal being proportional to the laser intensity. (b) In two-photon excitation, fluorescence occurs only at the focal area due to the nonlinear effect. This provides the intrinsic optical sectioning capability compared to single-photon excitation. (Figure adapted from https://xu.research.engineering.cornell.edu/research/)

2.2 Diffractive optical element (DOE)

Although 2PM provides multiple advantages, the speed limitation is restricted since it requires scanning through the whole sample (Fig. 2.2.1a). One way to increase the

21

imaging speed is to utilize multifoci, as mentioned in section 1.2.3, we have chosen DOE to form a scanless method.
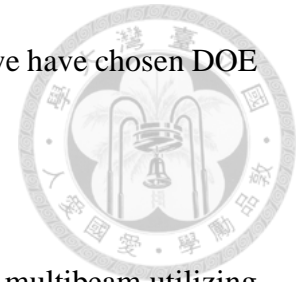
DOE is a phase element that splits a single beam from the laser into multibeam utilizing diffraction. The micro-structure embedded in the element transforms the beam shape into specific patterns, including beam array. The pattern is decided through simulating the diffractive result before manufacturing; thus, the pattern is fixed after it is produced. DOE also has nice performance with ~99% transmission rate, ~80% splitting efficiency and uniformity less than 1%, which is suitable since we require high intensity laser power for two-photon excitation. Here, we customized a DOE to form 32 beams in one direction. As shown in Fig. 2.2.1b, combined with a 1D galvanometric mirror, this parallel scanning enhances the imaging speed at least 32 times faster. To form a high-speed volumetric image, we need to combine this to a high-speed axial scanning technique.
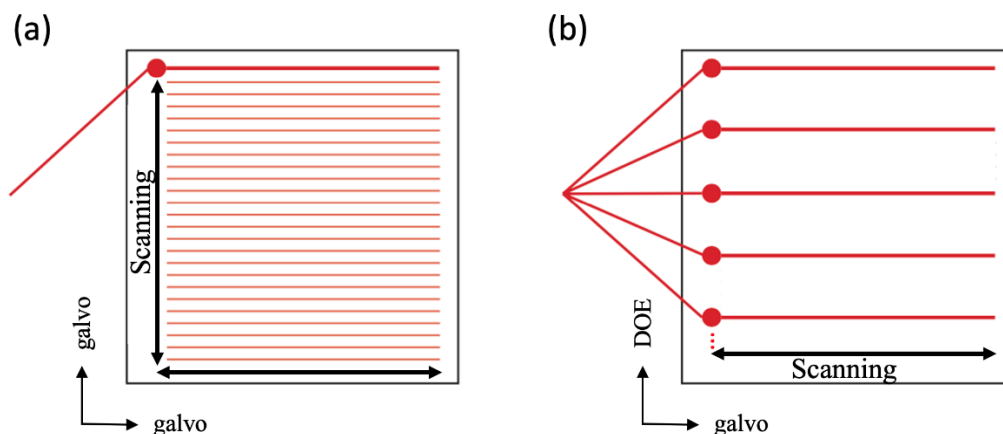
Fig. 2.2.1 The schematic of single beam and multibeam

(a) Traditional single beam scanning in 2PM requires single beam scan through the whole plane, resulting in relatively slow imaging speed. (b) DOE simultaneously generates multiple beams to cover one axis, this scanless method on the axis enhances the imaging speed. (Figure adapted from [46])

22
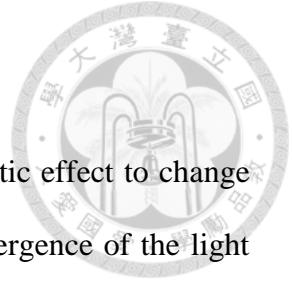
2.3 TAG lens

The tunable acoustic gradient-index (TAG) lens utilized acousto-optic effect to change the wavefront of the incident laser, resulting in convergence or divergence of the light passing through the lens. As shown in Fig. 2.3.1, the TAG lens is composed of silicone oil in the center surrounded by a cylindrical-shaped piezoelectric transducer, and an outer metallic housing [63]. When a TAG lens is operating, a sinusoidal voltage signal with specific frequencies drives the piezoelectric transducer, it then vibrates and creates acoustic standing waves inside the silicone oil, thus periodically changing the density of the oil. Which means the refractive index of the TAG lens is a spatial and temporal dependence function and is described as:

$$n(r,t) = n_0 + n_\alpha J_0\left(\frac{\omega r}{v}\right) sin(\omega t) \tag{2.1}$$

where n_0 is the static refractive index, n_α is the maximum refractive index when the lens is operating, J_0 is the Bessel function of the first kind, ω is the lens driving frequency, and v the speed of sound in the medium [64].

Fig. 2.3.1 Component of the TAG lens [63]

23

In an oscillation period, there are three stages during TAG lens operating, as shown in Fig. 2.3.2a, corresponding to the values of $sin(\omega t)$ in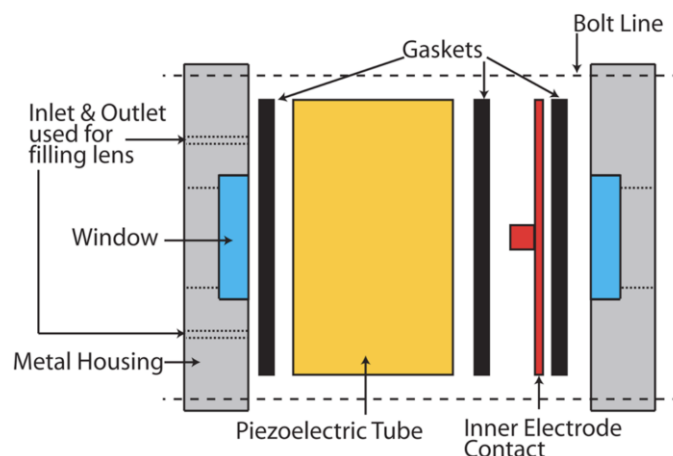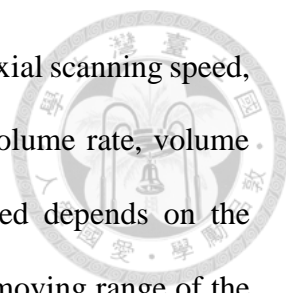 Eq. 2.1. The refractive index maintain uniform in TAG lens when $sin(\omega t) = 0$, thus the wavefront is unchanged and the position of the focus is at the z_0 image plane after the objective. When $sin(\omega t) > 0$, central refractive index has a local maximum, thus converges the incident beam, creating a focus at the z_1 image plane after the objective. On the contrary, when $sin(\omega t) < 0$, refractive index generates a local minimum at the central part, thus diverges the incident beam, creating a focus at the z_2 image plane after the objective. In brief, TAG lens acts like a convex and concave lens sinusoidally changing in between. After combining the TAG lens with an objective, the focus moves between z_1 and z_2, which forms the total axial scanning range (Δz), as shown in Fig. 2.3.2b. The frequency of the focus moving on the axial axis is identical to the driving frequency of the TAG lens.

By considering tube lens, TAG lens and objective, we determine the microscope scanning range. Assume the TAG lens as a tunable focal length lens with optical power changing from δ_{TAG} to $-\delta_{TAG}$. Via thin lens approximation and geometrical optics, the axial scanning range Δz is written as:

$$\Delta z = |z_1 - z_2| = \frac{2f_{tube}^2 \delta_{TAG}}{M^2 - \delta_{TAG}^2 (Md - f_{tube})^2} = \frac{2\delta_{TAG}}{\delta_{obj.}^2 - \delta_{TAG}^2 (\delta_{obj.} d - 1)^2} \quad (2.2)$$

where f_{tube} being focal length of the tube lens, δ_{TAG} and $\delta_{obj.}$ is the optical power of the TAG lens and objective, correspondingly, M the magnification of tube lens and objective and d is the distance between the TAG lens and the objective [65].

24

There are three important parameters in the TAG lens, which are the axial scanning speed, axial scanning range and the effective aperture, corresponding to volume rate, volume size and resolution. As mentioned previously, axial scanning speed depends on the driving frequency of the acoustic wave; axial scanning range is the moving range of the focus, as shown in Eq. 2.2. The effective aperture of the TAG lens is defined by the main lobe of the Bessel function, since only this region works like a periodically changing concave and convex lens, as shown in Fig.2.3.2a. Notice that there are relations between these parameters. In order to achieve high-speed volumetric imaging, higher driving frequency is recommended to increase the axial scanning speed, this also enhances the axial scanning range [66]. However, driving frequency ω will also affect the effective aperture, i.e. the Bessel function of the first kind, as shown in Eq. 2.1. In brief, the relation between these parameters are closed to each other and should be carefully chosen for individual applications.
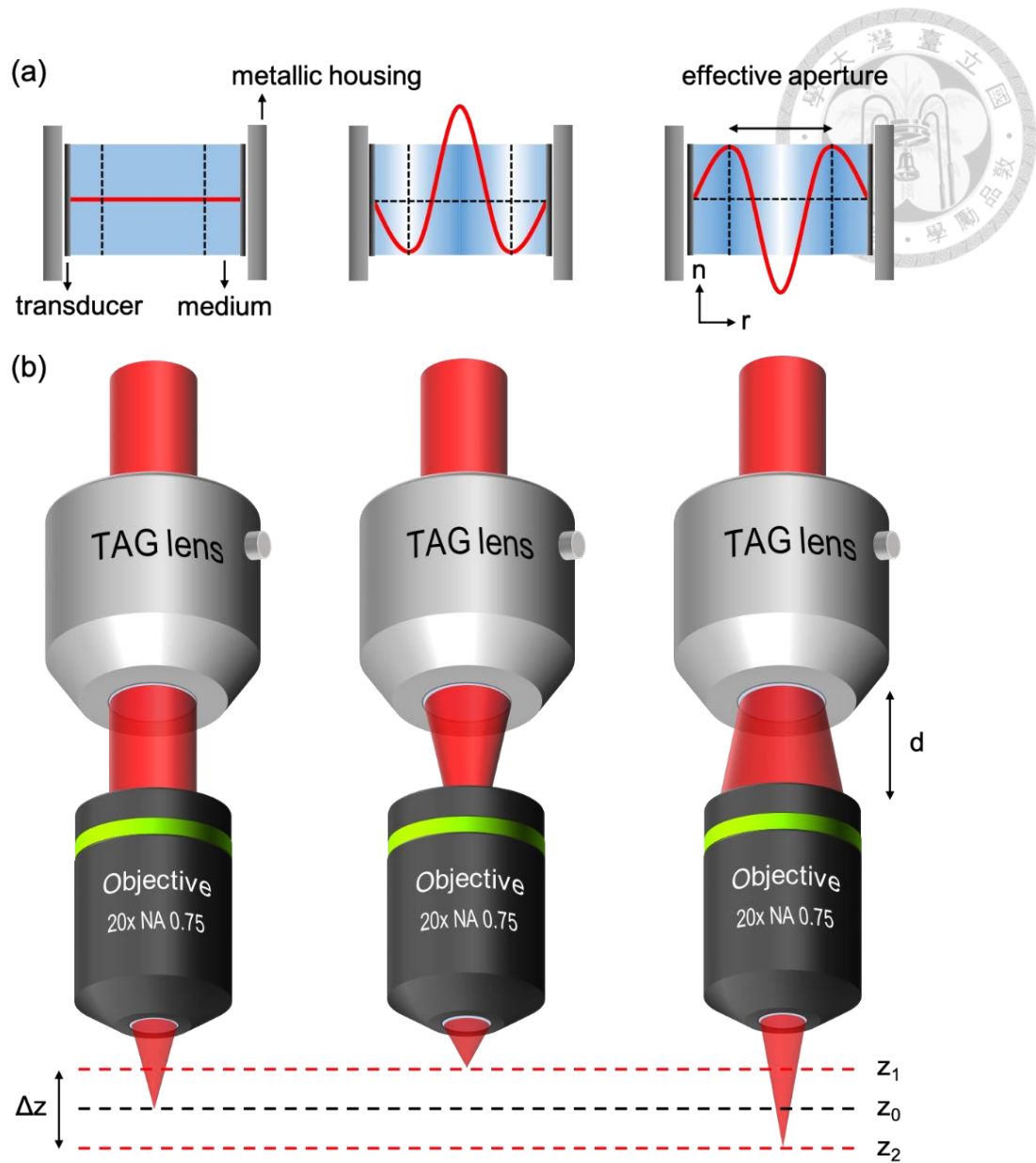
Fig. 2.3.2 Schematic of TAG lens and the objective achieving axial scanning

(a) Three stages of TAG lens which acts like a window, convex and concave lens. Red

curve is the profile of the refractive index. (b) Combination of TAG lens and objective

generating focus scanning on the axial axis between z_1 and z_2. r, radial coordinate along

lens radius; n, refractive index; d, distance between objective and the TAG lens; Δz,

total axial scanning range. [27]

2.4 High speed two-photon volumetric microscopy
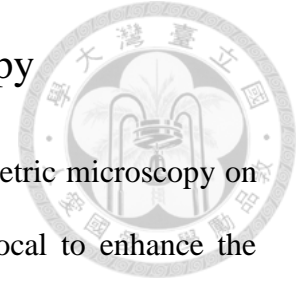
In summary, we increase the volume rate of our two-photon volumetric microscopy on two axes. On the lateral axis, DOE is utilized to generate multifocal to enhance the imaging speed. On the axial axis, TAG lens offers a high-speed focal scanning. After combining these two techniques with a 1D galvanometric mirror which is often used at laser scanning microscopy, this then achieves a high-speed volumetric microscopy, as shown in Fig. 2.4.1. Notice that the scanning frequency of the TAG lens is way higher than the galvanometric mirror. Instead of scanning the x-y plane first, the scanning order starts from the x-z plane, thus generating a vertical imaging plane, then moves to the next plane via the galvanometric mirror. This subsequently vertical imaging plane forms a volumetric imaging.
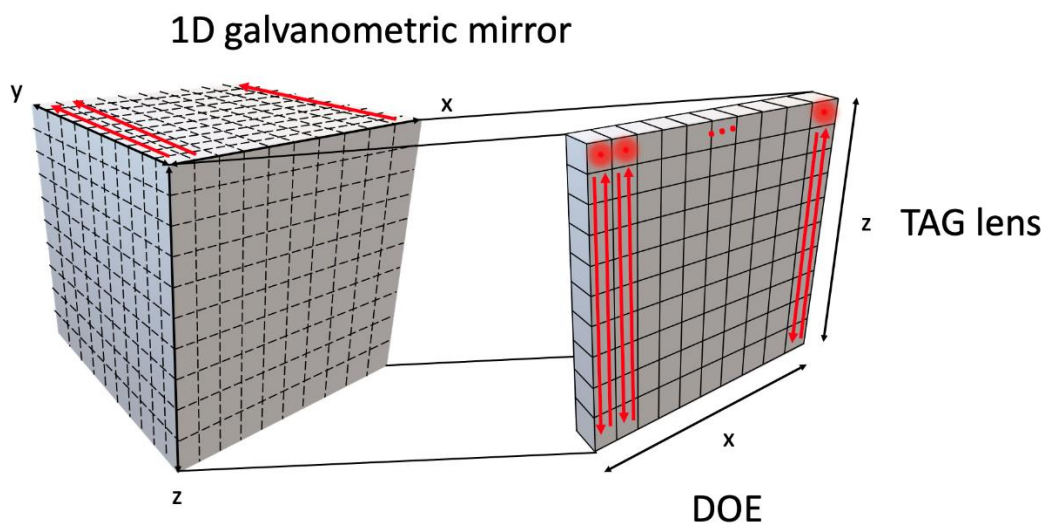
Fig. 2.4.1 Schematic of multifocal method combing with TAG lens achieving

volumetric microscopy

DOE generates a scanless method which covers the x direction, y direction is scanned

by a galvanometric mirror and TAG lens offers scanning on z direction

(Figure adapted from [27])

Chapter 3. Experimental method: system design and sample preparation

In the previous chapter, the principle of each technique forming a high-speed volumetric MMM was explained. Here, the information on how we composed our microscope will be demonstrated, including the optical and hardware setup, experimental protocol. The preparation of the *Drosophila* sample for functional imaging will also be displayed.

3.1 Optical setup

First, we will introduce the optical elements in optical setup following the light path, from excitation to emission. The overall schematic of our volumetric MMM is shown in Fig. 3.1.1.

Fig. 3.1.1 Schematic of high-speed volumetric MMM

HWP, half-wave plate; PBS, polarizing beam splitter; PMT, photomultiplier tube; Obj., objective. Image courtesy: G.-J. Huang.

A Ti:Sapphire pulsed laser (Chameleon Ultra II, Coherent) operates at 940 nm with an average output power of ~1.4 W, 140 fs pulse width and 80 MHz repetition rate is utilized for two-photon excitation laser source. Placing a pair of half-wave plate (HWP)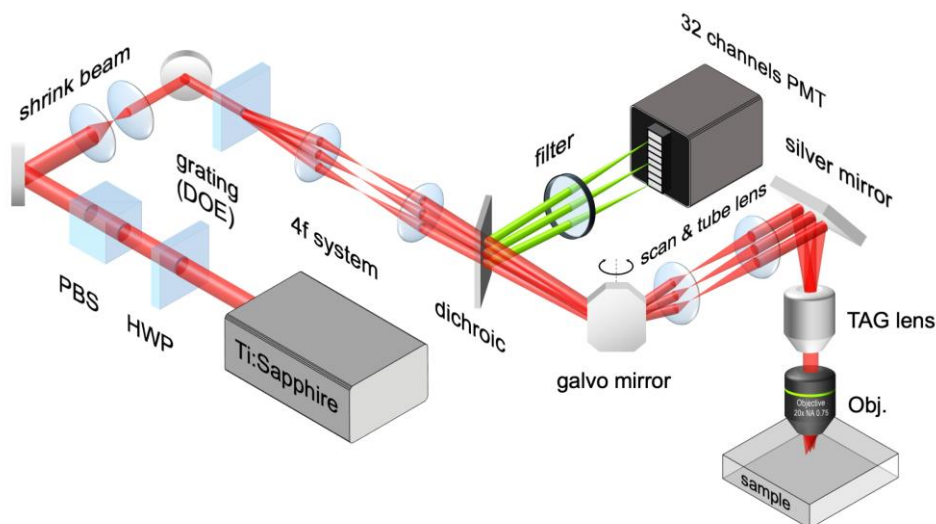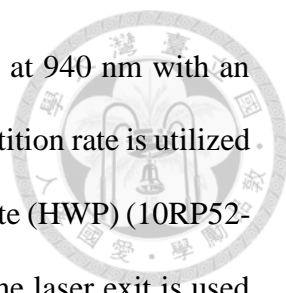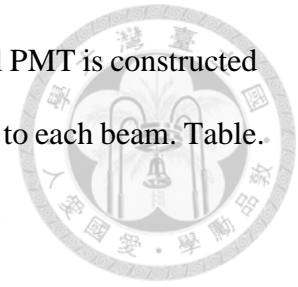 (10RP52-4, Newport) and polarizing beam splitter (PBS253, Thorlabs) after the laser exit is used for modifying the laser power. A pair of beam shrinkers (AC254-150-B-ML, AC254-50-B-ML, Thorlab) create a suitable beam size to fit the effective aperture of the TAG lens. With a customized diffractive optical element (DOE, Holo/Or), a single beam was splitted into 32 beams. A 4f system (AC254-100-B-ML, AC254-150-B-ML, Thorlab) then relays these beams onto the galvanometric mirror (6215HM40B, Cambridge Technology) for lateral scanning. These scanning beams are then sent through pair of telecentric scan and tube lens (SL50-CLS2, TL100-CLS2, Thorlab) to arrive the objective (HC PL IRAPO 20x, NA=0.75, water immersion, Leica) creating a multiline image. To achieve high speed axial scanning, the TAG lens (TAG Lens 2.5β, TAG Optic Inc.) operating at ~70 kHz was arranged before the objective to change the wavefront of 32 beams. Resulting in 32 foci simultaneously scanning in the z direction at ~70 kHz according to the states of the TAG lens. These 32 foci scan through the whole sample with the scanning directions of TAG lens and galvanometric mirror both orthogonal to the arrayment of the foci.

Epi-detection was used in this system, where the emitted fluorescent passed through the same objective, TAG lens and scan/tube lens. The signals are then descanned by the galvanometric mirror and separated via a dichroic mirror (DMLP650R, Thorlab). With a descanned method, the signals remain stationary on the detector. To filter out the laser and decrease the background signals, two band-pass filters (FF01-520/15-25, Semrock; FBG39-2IN-SP, Thorlab) are utilized before the detector. Since 32 foci simultaneously creates fluorescent signals, instead of using single-channel PMT for detection, a 32-

channel PMT (H12175-200, Hamamatsu) is utilized. This 32-channel PMT is constructed by a lineup of single-channel PMTs with each channel corresponding to each beam. Table. 3.1.1 shows the manufacturer and model number of each instrument.

Instrument	Manufacturer	Model number
Ti:Sapphire Laser	Coherent	Chameleon Ultra II
Half-wave plate	Newport	10RP52-4
Polarizing beam splitter	Thorlabs	PBS253
Beam shrinkers, lens 1	Thorlabs	AC254-150-B-ML
Beam shrinkers, lens 2	Thorlabs	AC254-50-B-ML
Diffractive optical element	Holo/Or	Customized 32-beam splitter
4f system, lens 1	Thorlabs	AC254-100-B-ML
4f system, lens 2	Thorlabs	AC254-150-B-ML
Galvanometric mirror	Cambridge Technology	6215HM40B
Scan lens	Thorlabs	SL50-CLS2
Tube lens	Thorlabs	TL100-CLS2
Silver mirror	Thorlabs	PF20-03-P01
TAG lens	TAG Optics Inc.	TAG lens 2.5β
Objective	Leica	HC PL IRAPO 20x/0.75 W
Z stage	OptoSigma	GSC-01
Dichroic	Thorlabs	DMLP650R
Filter	Semrock	FF01-520/15-25
Filter	Thorlab	FBG39-2IN-SP
32-channel PMT	Hamamatsu	H12175-200

Table 3.1.1 Manufacturer and model number of the instruments.

In 2PM for neuroimaging, fluorescent proteins are often used to increase the imaging contrast [67]. Among several kinds of fluorescent proteins, green fluorescent proteins (GFP) provide comparatively large two-photon cross-section and mature development, thus are one of the suitable candidates [68]. Lately, jGCaMP7, a family of GFP-based calcium sensors has better performance than other sensors to detect activity responses of neurons, for example, jGCaMP7f has higher intermediate kinetics than GCaMP6f [69]. Since the maximum two-photon cross-section of jGCaMP7 is around 940 nm, as shown in Fig. 3.1.2, we choose 940 nm for our excitation wavelength.
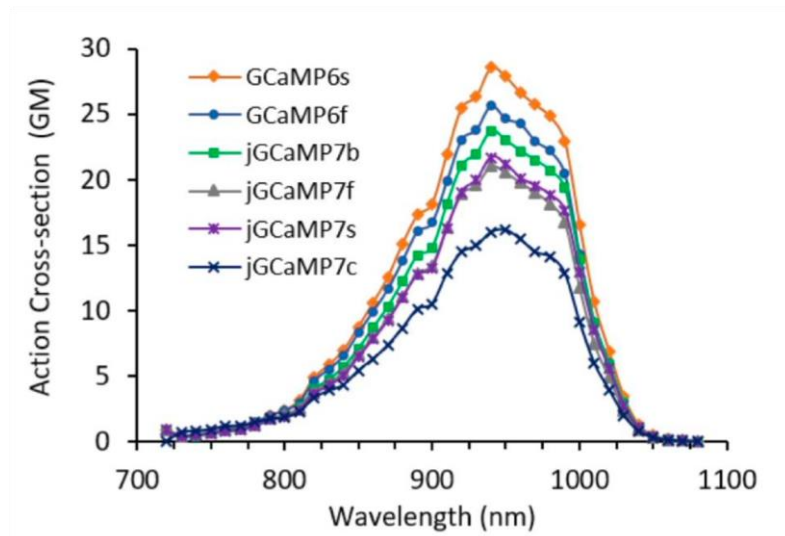
Fig. 3.1.2 Two-photon excitation cross-section of jGCaMP7 family [69]

The excitation laser passes through the DOE to form a multifoci, as we mention from section 2.2, the parameters are fixed once the DOE was fabricated. Hence, we need to choose the parameters of DOE to match our sample, *Drosophila*. Since the size of the *Drosophila* brain is $\sim 200 \times 700$ µm^2. The short side (200 µm) must be covered by multifoci to achieve whole brain imaging. Due to the neuron size of *Drosophila* is about 6 µm [26], we deduce that 32-33 neurons are on the short side of *Drosophila* brain. Thus, we separated 32 foci with 6.875 degree splitting angle, so that every neuron is at least

31

scanned by one beam. Combining DOE with 4f system, scan/tube lens and the 20x objective with 10 mm focal length, the 6.875 degree splitting angle is enough to cover 200 µm. The calculation is shown as:
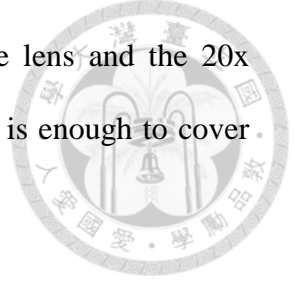
$$Full\ range = f_{obj.} \times \theta_{DOE} \times M_{4f} \times M_{s/t} \qquad (3.1)$$

$$= 10\ mm \times \left(6.875° \times \frac{\pi}{180}\right) \times \frac{100}{150} \times \frac{50}{200}$$

$$= 200\ µm$$

where $f_{obj.}$ is the focal length of the objective, θ_{DOE} is the splitting angle of the DOE, M_{4f} is the magnification of 4f system, $M_{s/t}$ is the magnification of the scan/tube lens. The long side is simply scanned by 1D galvanometric mirror with maximal scanning range achieving ~850 µm [27], with the combination of DOE and galvanometric mirror, we are able to cover the lateral plane of the *Drosophila* brain, as shown in Fig. 3.1.3.
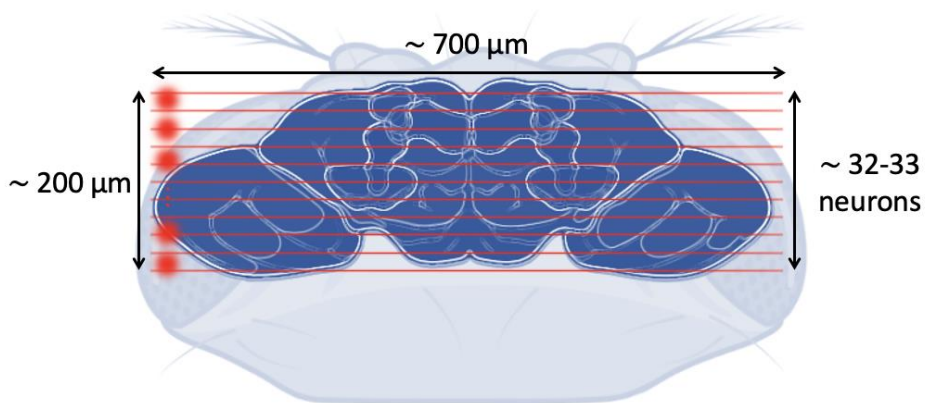

Fig. 3.1.3 Schematic of multifoci combining with galvanometric mirror scanning

through the lateral plane of the *Drosophila* brain

DOE forms 32 foci (red spots) aligned on the short side while 1D galvanometric

mirror scans the foci on the long side (red lines), covering the lateral plane of the

Drosophila brain (dark blue) (Created with BioRender.com.)

32

After introducing the specification of DOE, which increases the lateral imaging speed. The following paragraph we determined the parameter of the TAG lens that achieves high speed axial scanning. Here, we placed the TAG lens just in front of the objective to optimize DOF extension and signal collection efficiency [64], therefore, we need to consider the effective aperture of the TAG lens. Due to the fact that small effective aperture causes small beam size incidents on the back aperture of the objective, leading to lower NA and decreasing the spatial resolution. Since the back aperture of our objective is ~16 mm, we selected the maximal effective aperture of our TAG lens, which is ~11 mm for our microscope (Table. 3.1.2). The corresponding frequency is ~70 kHz with total lens power 2 m^{-1}.

Frequency (kHz)	Calc. Eff. Aperture (mm)	Total Optical Power (diopters)	% of Max Driving Amplitude
68.5	11.0	0.5	20%
68.5	11.0	1.0	39%
68.5	11.0	1.5	58%
68.5	11.0	2.0	75%
188.0	4.0	10.0	43%
188.0	4.0	20.0	80%
308.0	2.5	10.0	5%
308.0	2.5	20.0	10%

Table 3.1.2 Specification of TAG Lens 2.5β.

The value of axial scanning range is shown in Eq. 2.2, by utilizing a 10 mm focal length objective lens, we theoretically achieve ~200 µm depth coverage.

$$\Delta z = \frac{2\delta_{TAG}}{\delta_{obj.}^2 - \delta_{TAG}^2 (\delta_{obj.}d - 1)^2} \qquad (3.2)$$

$$= \frac{2}{100^2 - (100 \times 0.005 - 1)^2} \, m = 200 \, \mu m$$

33

Since the axial length of *Drosophila* is ~360 µm, the axial scanning range of the TAG lens seems unable to cover the whole z direction. Fortunately, the experimental scanning range, done by our former member Yu-Hsuan Tsai, is about 80% larger than the theoretical result, which is able to extend to ~360 µm [27], thus the TAG lens scanning range is enough to cover the axial length of *Drosophila* (Fig. 3.1.4).
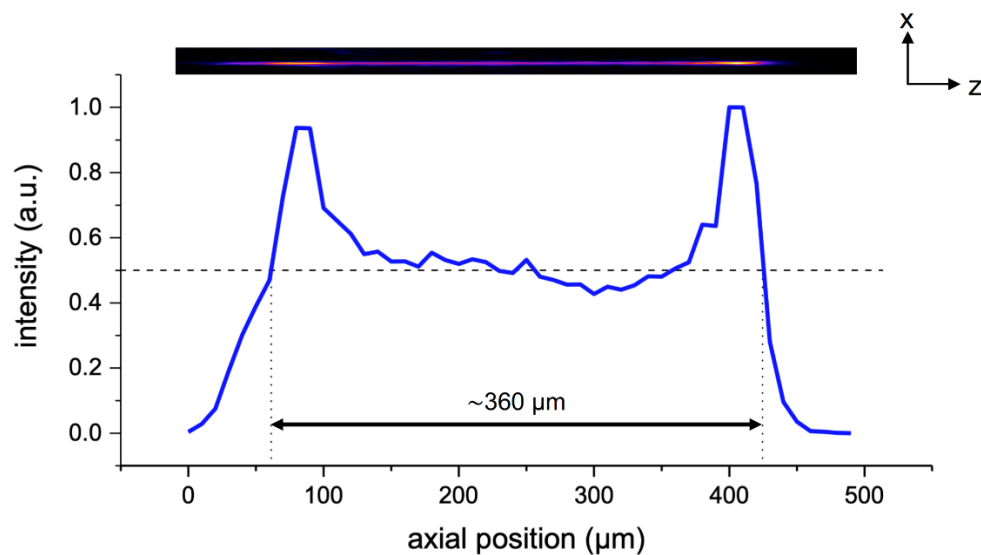

Fig. 3.1.4 The experimental axial scanning range of the TAG lens

(Figure adapted from [27])

The above paragraph shows that the volume size is large enough to cover the whole *Drosophila* brain, we then simply go through the temporal resolution of our high-speed microscopy. Since the frequency of the TAG lens operates at ~70 kHz, we easily calculate the time of the foci scans through the whole volume. As mentioned in section 2.4, the foci first scan the z axis with the same frequency as the TAG lens then moves to the adjacent vertical plane by the galvo mirror. In our system, we are able to choose different pixel numbers on the galvo scanning axis, such as 128, 256, 512 and 1024. Notice that with
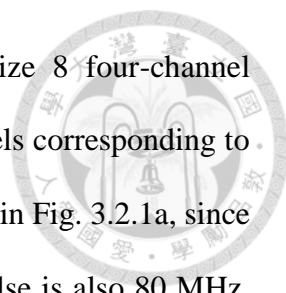
larger pixels, it causes longer scanning time. Take 128 pixels for example, the scanning

time t is calculated as:

$$t = T_{TAG} \times N_{pix.} \tag{3.3}$$

$$= \frac{1}{70k} \times 128 \, s = 1.8 \, ms$$

where T_{TAG} is the period of the TAG lens, and $N_{pix.}$ are the selected pixel numbers on the

galvo scanning axis. Thus, we achieve a high temporal resolution microscopy (~1.8 ms)

with the volume rate >500 volumes/second.

3.2 Hardware setup

In our microscope, we use PMT to detect the emitted photons and transfer optical signals

to current signals. Since the emitted photon yield per pulse is only ~3 photons/pulse, we

choose a maximal quantum effect PMT (H12175-200, Hamamatsu) with ~20% as our

detector [27], which is a 32-channel PMT. This then outputs a ~µA current which is too

small for data acquisition. Thus, we customized two 32-channel amplifier boards (AMP)

with the assistance of Southport Co., Ltd, to magnify the signals of the PMT. The first

AMP board composed of 32 ERA-3SM+ (Mini-Circuits) connects just behind the PMT,

after that the signals transfer by 32 SMA-SMA cables to the second AMP board

composed of 32 ADRF6520 (Analog Devices), with 23.5 dB and 53 dB maximal gain

correspondingly. This not only increases the current signals, but also avoids the electrical

crosstalk during signal transforming, the detailed introduction will be discussed at section

4.4.2.

After the current signals are magnified with amplifiers, we utilize 8 four-channel digitizers (NI-5734, National Instrument), so that we have 32 channels corresponding to 32 foci-induced fluorescence signals. The overall data flow is shown in Fig. 3.2.1a, since the repetition rate of the pulse laser is 80 MHz, the fluorescence pulse is also 80 MHz. The maximum sampling rate of our digitizer is 120 MS/s (sample per second), which is high enough for our sampling. The sampling time of data acquisition is triggered by the synchronization signal from the Ti:Sapphire laser we use, which is also 80 MHz. Before the synchronization signal is imported into the digitizer, it passes through a delay board in order to match the maximum fluorescence signals. Since every fluorescence signal is input into the digitizer, the total throughput for each digitizer is 320 MS/s with 16-bit sampling size, thus the data throughput is too large. Here we utilize a field-programmable gate array (FPGA) (PXIe-7972, National Instrument) to not only down-sampling the sampling size from 16-bit to 8-bit but also pre-processing the data via decimation, accumulation or average (Fig. 3.2.1b). For example, after average N pixels via FPGA, the sampling rate per digitizer is $4\times80/N$ MS/s; and the data throughput per digitizer is $(4\times80/N)\times8$ Mbit/s, which is $4\times80/N$ MB/s. Since we use 8 digitizers, the total data throughput is $2.56/N$ GB/s, so an array of solid-state disk (HDD-8261, National Instrument) constructed into a redundant array of independent disks (RAID) offers 2 GB/s transmission rate is used for our data acquisition system (DAQ). Notice that N is chosen to be 1, 2, 4 or 8, this results in the pixel numbers on the z axis. In this study, we average 8 pixels in our system, leading to ~70 layers on the axial axis, which has quite large layers compared to other high-speed volumetric microscopes [53, 54]. The calculation of the layers on the z axis is shown as:

$$Layers\ on\ z\ axis = \Gamma \times T_{TAG} \div 2N \qquad\qquad (3.4)$$

$$= 80M \times \frac{1}{70k} \div 16 \approx 70$$

where Γ is the repetition rate of the laser pulse, T_{TAG} is the period of the TAG lens and N is the selected pixel numbers for pre-processing the data.

Since our receiving data is eight 1D arrays on the time sequence. We need to reconstruct the signals at the precise position to generate a 3D volumetric image. A transistor-transistor logic (TTL) signal synchronized with the operating frequency of the TAG lens, which is generated by the TAG lens controller, is imported into a multifunction I/O module (PXIe-6368, National Instrument) to record the position of the galvanometric mirror and the TAG lens for image reconstruction. The TAG TTL signal is also imported into the eight digitizers for synchronizing them together. These above instruments including the I/O module, digitizers were integrated into a computer case (PXIe-1075, National Instrument) and manipulated by a controller (PXIe-8880, National Instrument).
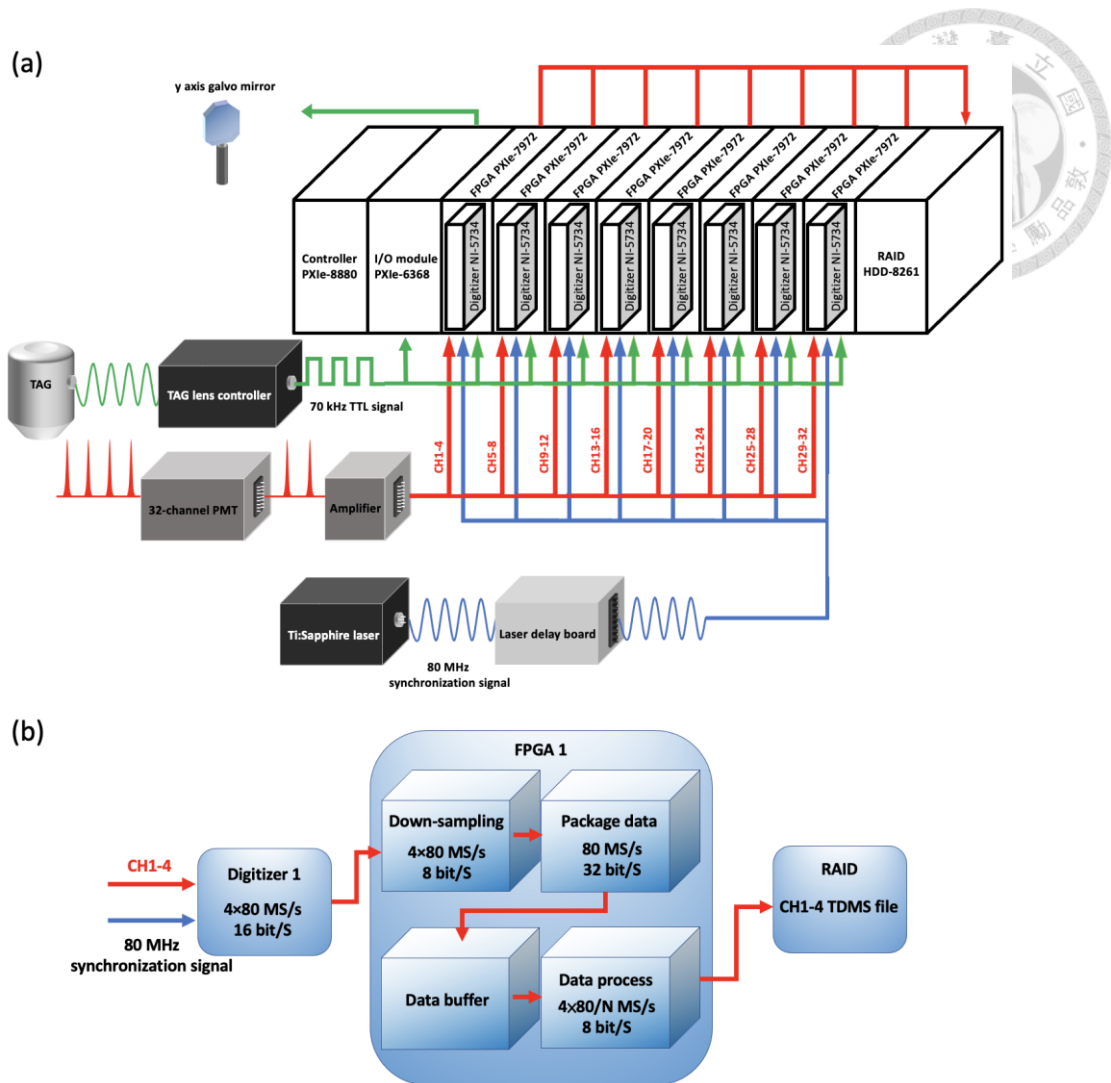
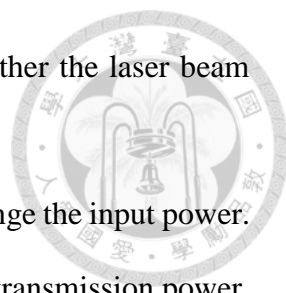Fig. 3.2.1 Overall data flow of our digital acquisition system

(a) Data and signal flow in the DAQ system. Blue line: Laser synchronization signal.

Red line: Fluorescent/data signal. Green line: TAG signal. (b) Utilizing FPGA for data

pre-processing. (Figure adapted from [27])

3.3 Experimental protocol

1. Excitation beam alignment of two-photon microscopy

   ● Turn Ti:Sapphire laser on and adjust the wavelength to 940 nm.

   ● Place the removable mirror on the beam path with a specific angle to lead

   the laser into our system.

38

- Turn on the Ti:Sapphire laser shutter and check whether the laser beam enters our system by an IR viewer.

- By adjusting the angle of the HWP, we are able to change the input power. Adjust the degree of the HWP to 79 degrees for least transmission power.

- Adjust the knobs of the mirrors to align the laser beam to pass the irises, which is called beam-walking. This makes sure the laser passes through the center of the optical elements, such as the 4f system and scan/tube lens.

- Screw the hollow tube which has two irises inside to the objective mount. Tune the knobs of the silver mirrors to align the laser beam to pass the center of the objective.

- Change the hollow tube to the objective into the lens mount.

- A single beam 2D imaging with a single channel PMT (PMT2100, Thorlab) is used to easily find the sample and spatially correspond to our high-speed multifocal microscope. Insert the dichroic (FF573-Di01-25X36, Semrock) which is mounted on a flipper between the scan/tube lens to guide the emission fluorescence into the single channel PMT. This is called slow scan imaging in the following article.

- Turn on the computer and click "PMT2100 4.0" to operate the single channel PMT for single beam 2D imaging. Click "JadeMAT 3.3" software to run the 2D imaging program. The parameters are adjustable such as image size, pixel dwell time. One can also change the z position or achieve a z stack image at the stage control region, as shown in Fig. 3.3.1. Then click "JadeMat Reader 2.1" to read the 2D image.
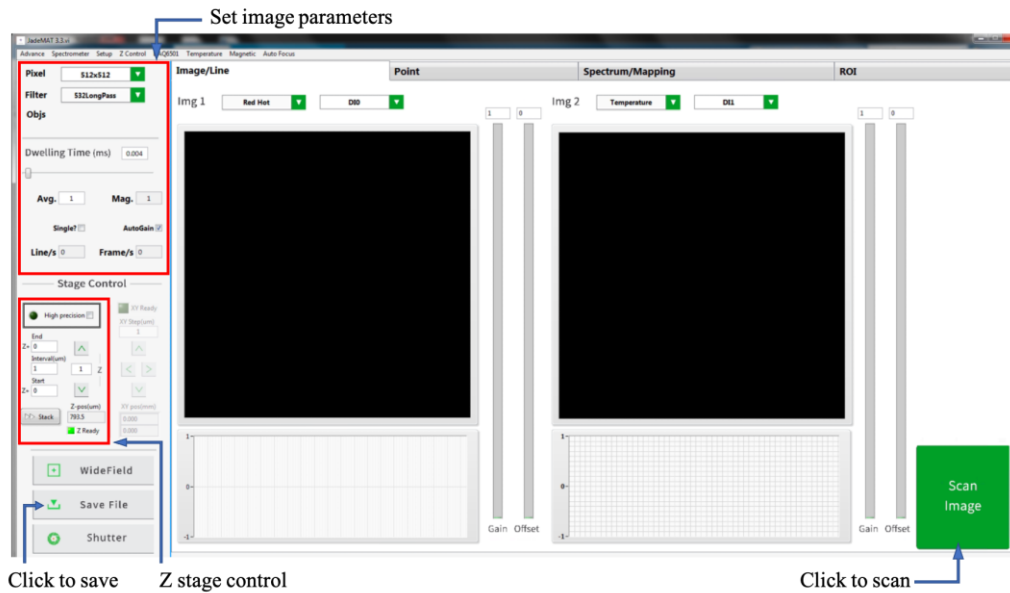
39

Fig. 3.3.1 Software of 2D imaging and the control panel of "JadeMAT 3.3"

2. Emission beam alignment of multifocal two-photon microscopy

- Place 1 mM FITC fluorescent liquid of a glass container under the objective.

- Tune the HWP to 70 degrees for 40 mW laser power after the objective to excite the fluorescent liquid.

- Remove the dichroic between the scan/tube lens which is for single beam scanning.

- Insert the dichroic (DMLP650R, Thorlabs) between the 4f system and galvanometric mirror to guide the emission fluorescence into the multichannel PMT. Adjust the angle of the dichroic and the mirror after

40

the dichroic to align the detected light path and make sure it roughly locates at the center of the detector.

- Turn on the power of the multichannel PMT and the amplifier. Click the "32chs Amplifier.exe" to adjust the gain of the second amplifier (ADRF6520, Analog Devices) to 60% which provides ~30 dB gain (Fig. 3.3.2).

- Import the output cable of CH16 and CH17 from the AMP to the oscilloscope and balance the amplitude of the signals from two channels.
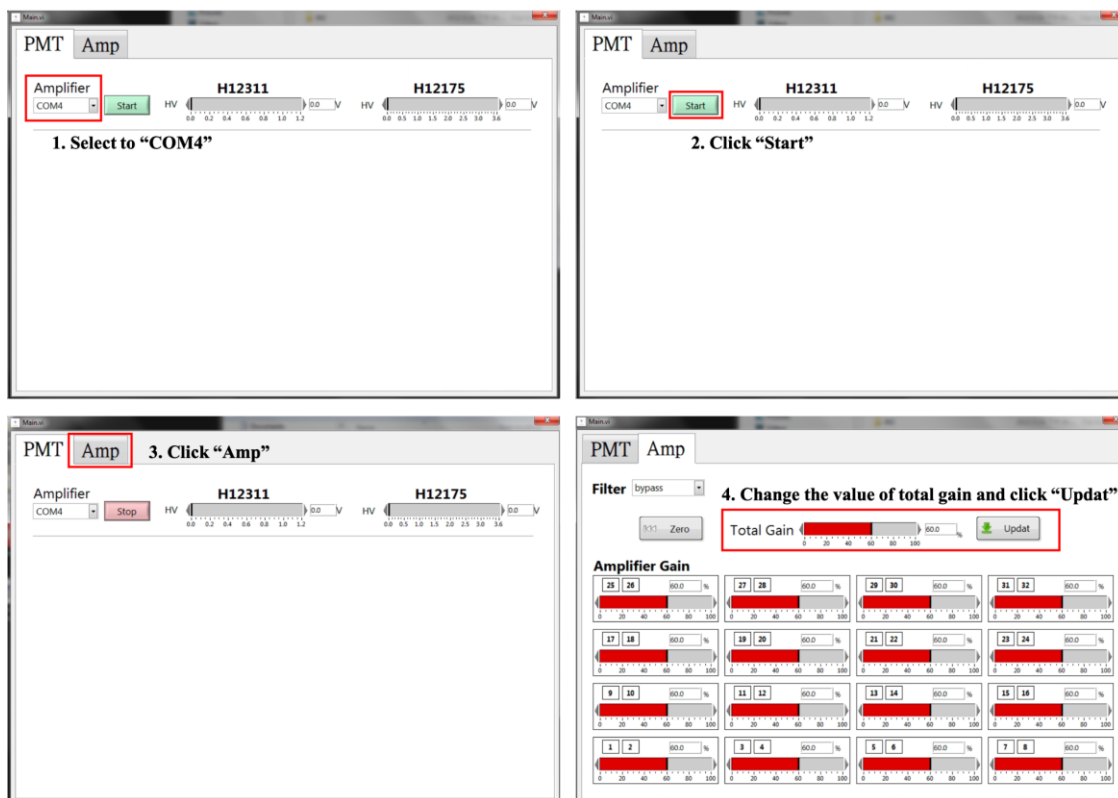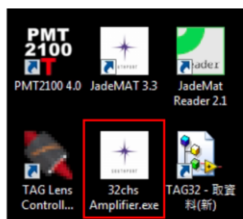

Fig. 3.3.2 Control panel of amplifier and its operation steps

3. Data acquisition

- Adjust the laser delay board to match the laser trigger and the fluorescent
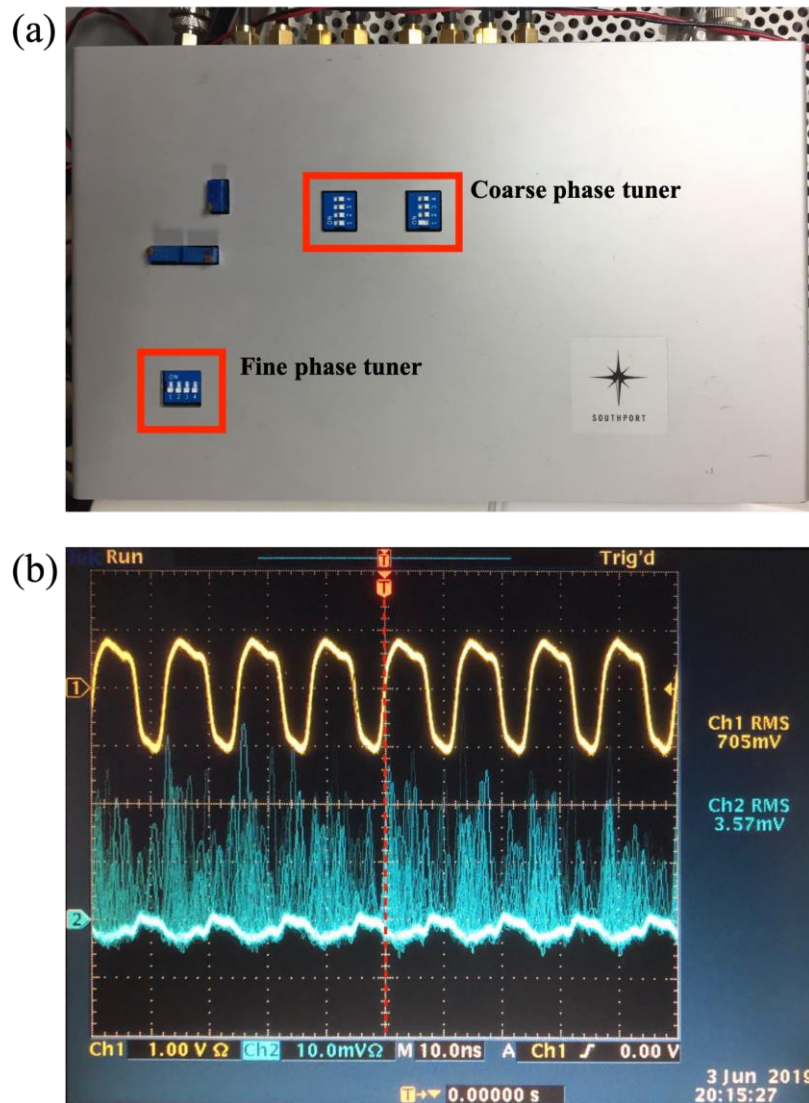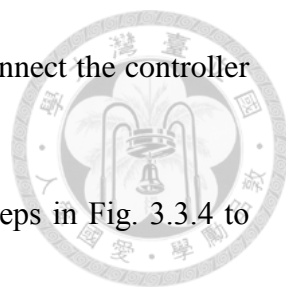
  peak (Fig 3.3.3)

.

Fig. 3.3.3 Laser delay board and the synchronized laser corresponding to the fluorescent

signals

(a) The coarse and the fine phase tuner is able to delay the synchronized laser. (b)

Synchronized laser (CH1) and the fluorescent signal (CH2) shown by an oscilloscope.

Red dot line is the sampling time which has to match the peak of

the fluorescent signals. [27]

42

- Turn on the power of the TAG lens controller and connect the controller to the TAG lens with a SMA connector.

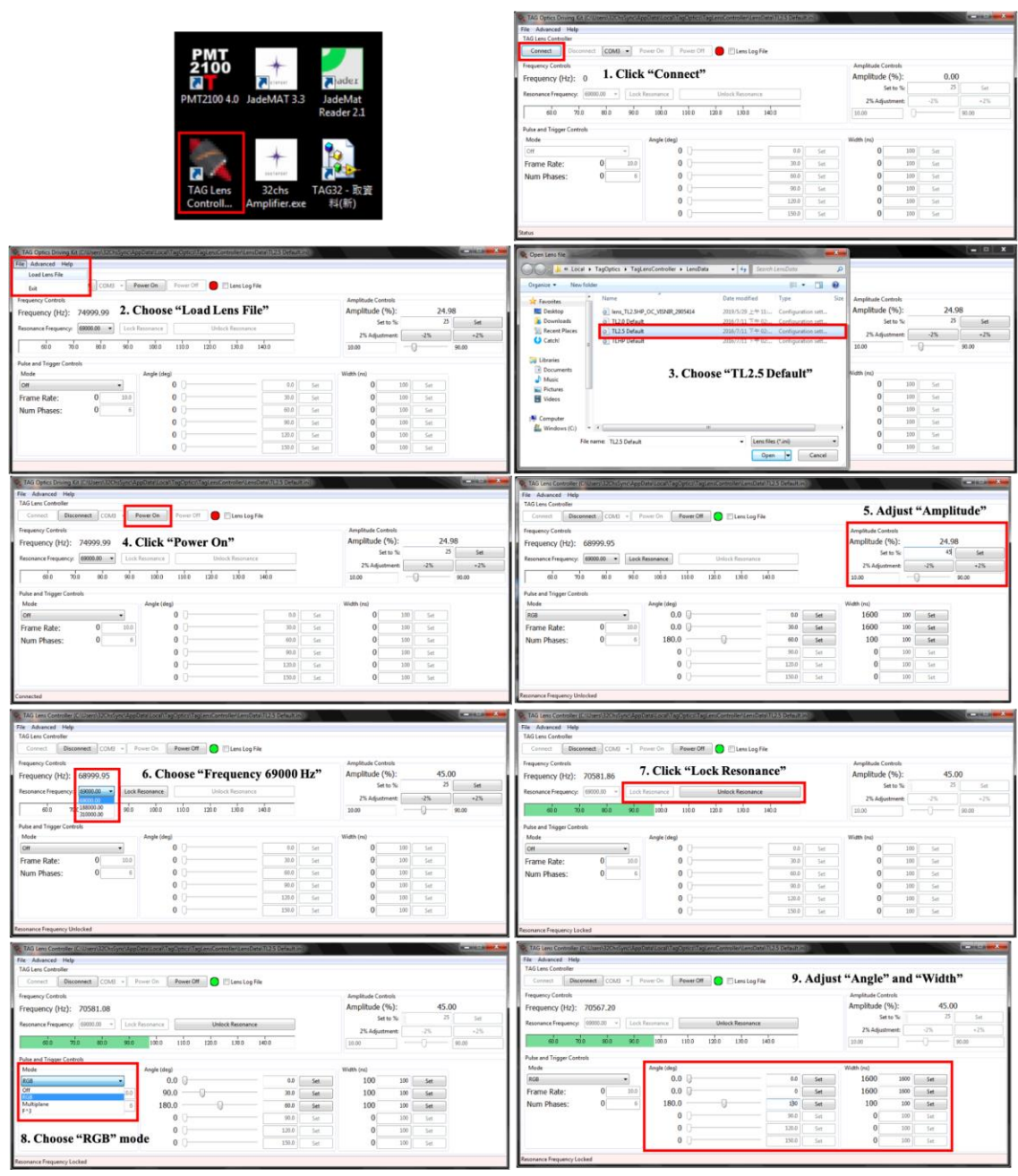- Click "TAG Lens controller 3.3.8" and follow the steps in Fig. 3.3.4 to operate the TAG lens.

Fig. 3.3.4 Operation steps of the TAG lens

(Figure adapted from [27])

43

- Insert the DOE which is mounted on a flipper.

- Replace the fluorescent liquid with a 3D fluorescent microsphere sample or *Drosophila* brain sample. Click the "TAG 32" software for data acquisition of 3D imaging on the computer and follow the steps in Fig. 3.3.5 to accomplish data acquisition of our high-speed volumetric imaging.

4. 3D image reconstruction

- Click "TAG32Parser_v1.1.exe" and follow the steps in Fig. 3.3.6 to reconstruct the volumetric imaging data.

- This software reconstructs the acquired data into multiple 2D images (x-y plane) in different z layers. Click "First=>PNG" and "ALL=>PNG" to save the first and every acquired volume, correspondingly. It transfers into DAT and PNG files from TDMS files and can be exported for further analysis.
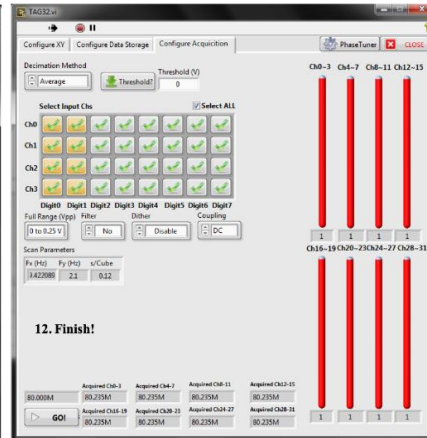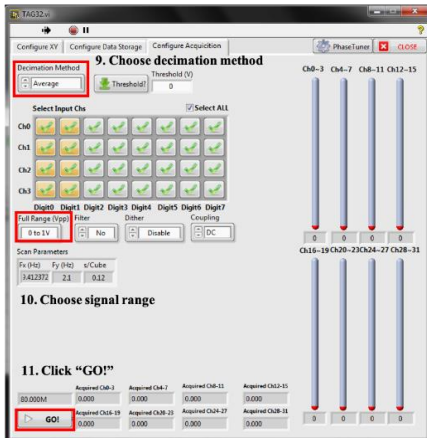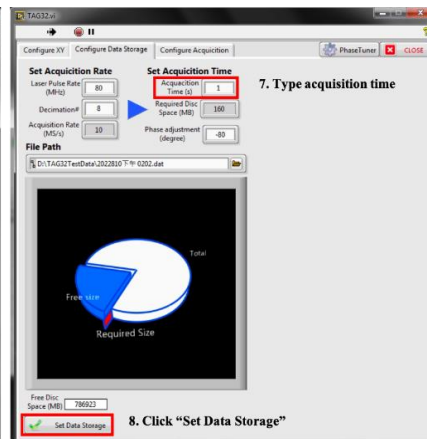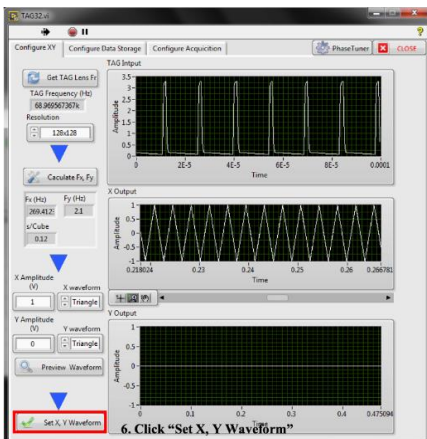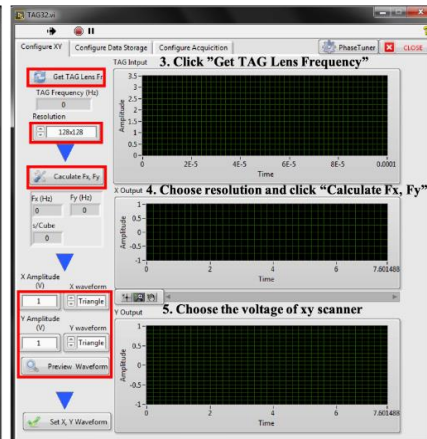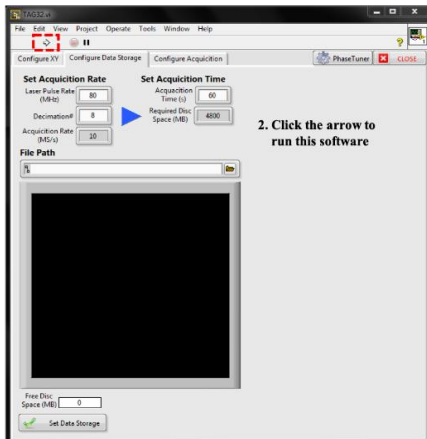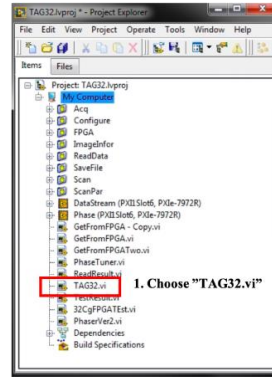
Fig. 3.3.5 Data acquisition software and operation steps

(Figure adapted from [27])

45
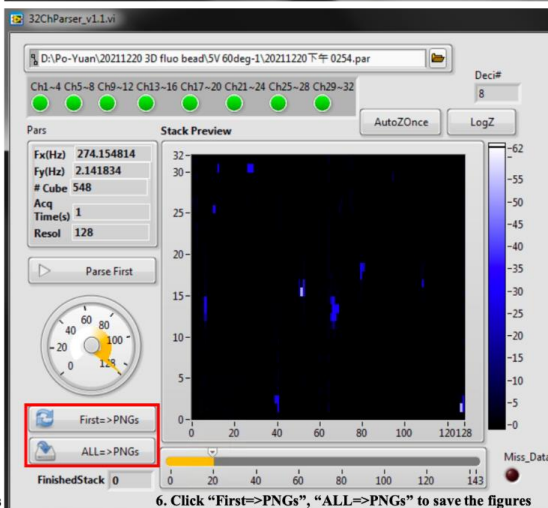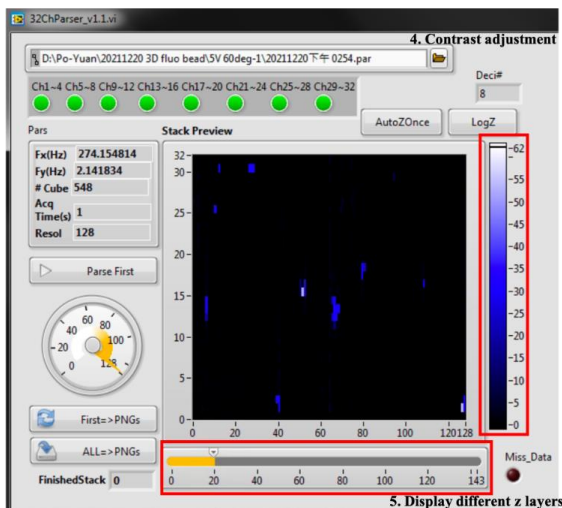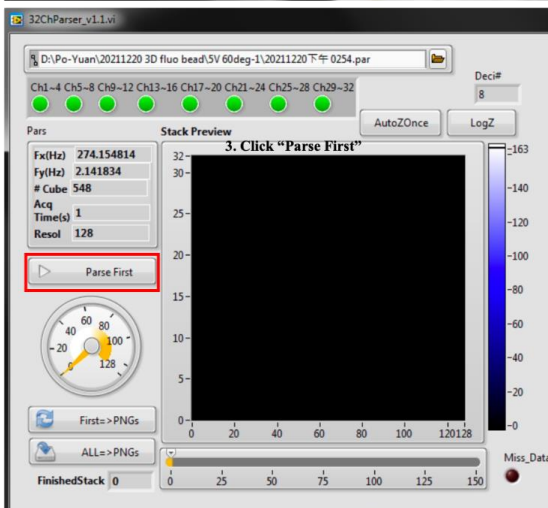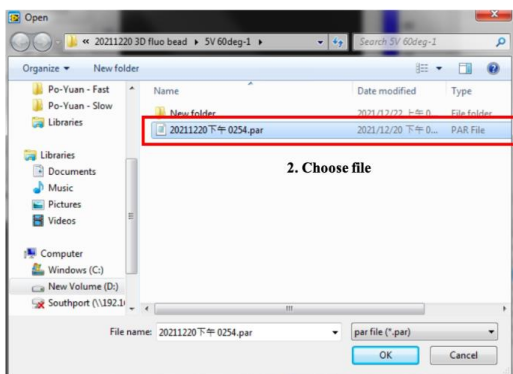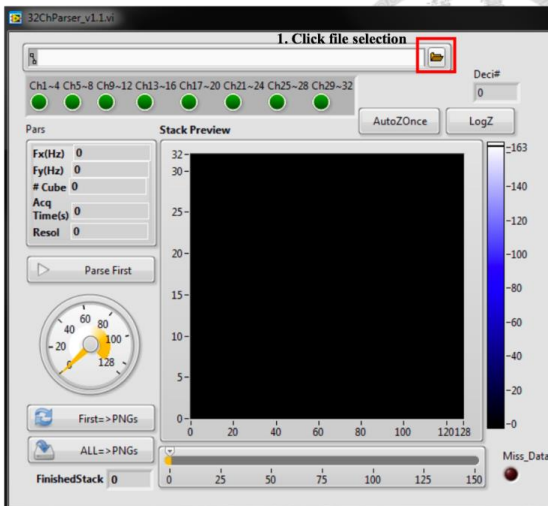
Fig. 3.3.6 3D image reconstruction software and operation steps

3.4 *Drosophila* sample: Electric shock
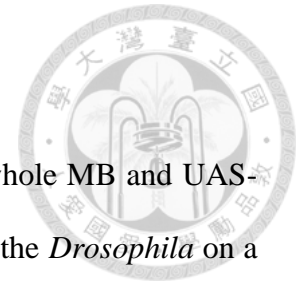
For the *Drosophila* fly line, we use OK107-GAL4 to express the whole MB and UAS-GCaMP7f for genetically encoded calcium sensors. We then mount the *Drosophila* on a homemade fly stage. The fly stage is made by MakerBot Replicator+ and embedded with an iron plate in the middle. The fly is placed into the ice bucket for 20 minutes for fainting, it then will be fixed on the iron plate with AB glue. After waiting the glue dries, add phosphate buffered saline to keep the fly alive. We then remove the cuticle of the *Drosophila* head by removing the skull by tweezers (Dumont #55) and the air sacs above the brain. The *Drosophila* brain is exposed below the objective and is ready for imaging.

In order to obtain functional study, here we use electric shock. We create a periodic voltage pulse by Arduino and relay, as shown in Fig. 3.4.1a. The DC power supply provides 25 voltages and the relay controlled by the Arduino generating voltage pulse with the duration of electric shock is 0.7 s and relaxing time is 1 s. The voltage pulses are sent to the *Drosophila* via two screws. One screw is connected to the iron plate and the other is connected to the *Drosophila* abdomen by iron wires. This allows the periodic electric shocks passing through the sample (Fig. 3.4.1b). Further details of brain surgery and activating the Arduino for electric shock is recorded in Hung-Yu Chen's master thesis [70].

(a)

Arduino

Relay

DC POWER SUPPLY

15.00 V

0.00 A

(b)

Drosophila
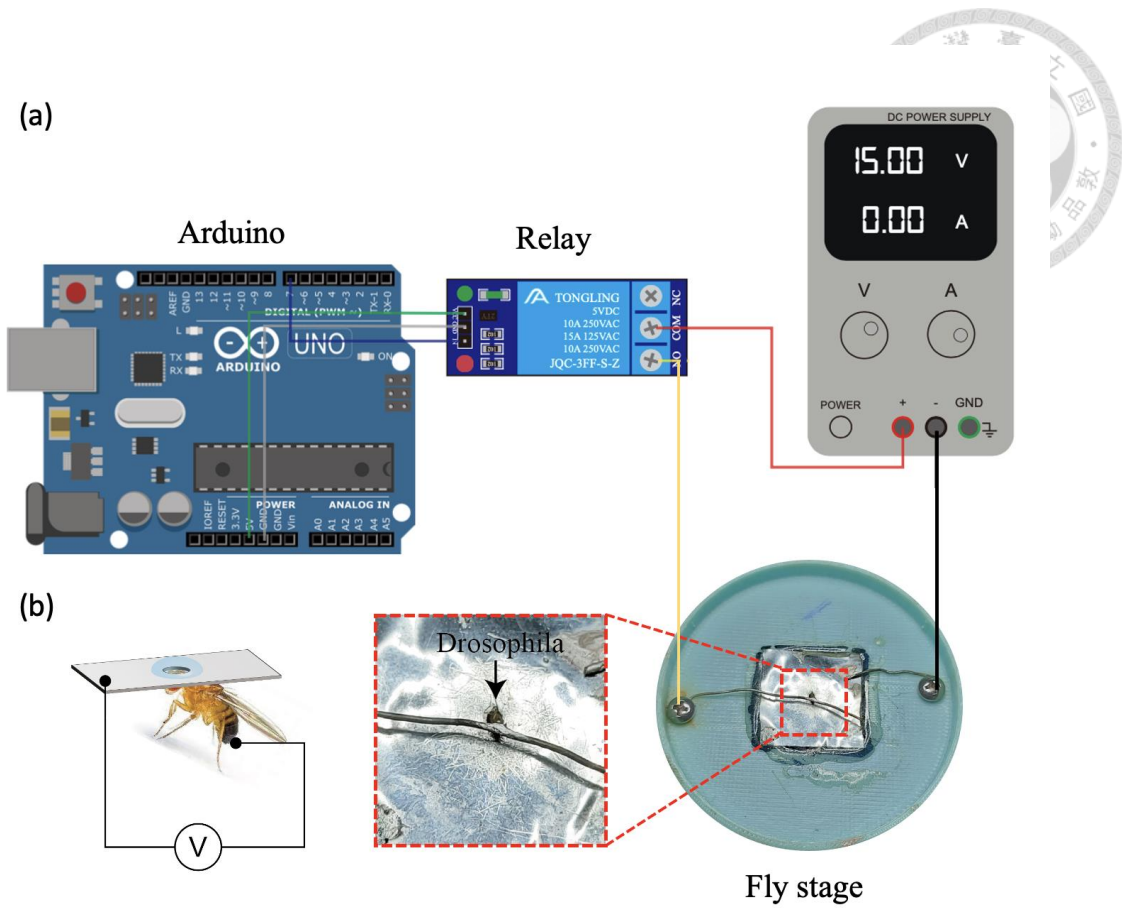
Fly stage

Fig. 3.4.1 Setup of electric simulation and fly stage

(a) DC power supply provides steady current with 25 V; the Arduino and relay

generates the voltage pulse. (b) The schematic of the circuit passes through the

Drosophila. (Figure adapted from [70])

Chapter 4. Improvement of the system and solutions

Although our microscope offers the highest speed in two-photon volumetric microscopy, this state-of-the-art system encounters some challenges, such as crosstalk due to multichannel and high data throughput that might cause missing data. In this chapter, we introduce the challenges we found and their solutions.

4.1 Crosstalk in multichannel

Even though multichannel PMT highly increases the imaging speed, the intrinsic drawback is the crosstalk between different channels [71]. Our lab member Chien-Sheng Wang utilized photon reassignment algorithm to solve this issue. Here, we use single-beam and a single-channel PMT to acquire a high-resolution image which is mentioned at section 3.3 excitation part (slow scan image). The step size is 60 nm on both x and y axis. The figure is shown in Fig. 4.4.1a. After switching to our high-speed multichannel microscope, the image shown in Fig. 4.4.1b is oval due to the crosstalk along the multichannel array (x axis). With improving the image based on photon reassignment algorithm via crosstalk vector, which is $[L^2\ L\ 1\ L\ L^2]$. The L is the percentage leaking to the adjacent channels. The optimization of the L value is obtained by manual iteration to approach the similarity of the slow scan image. With this photon reassignment algorithm, the crosstalk effect is decreased, as shown in Fig. 4.4.1c.
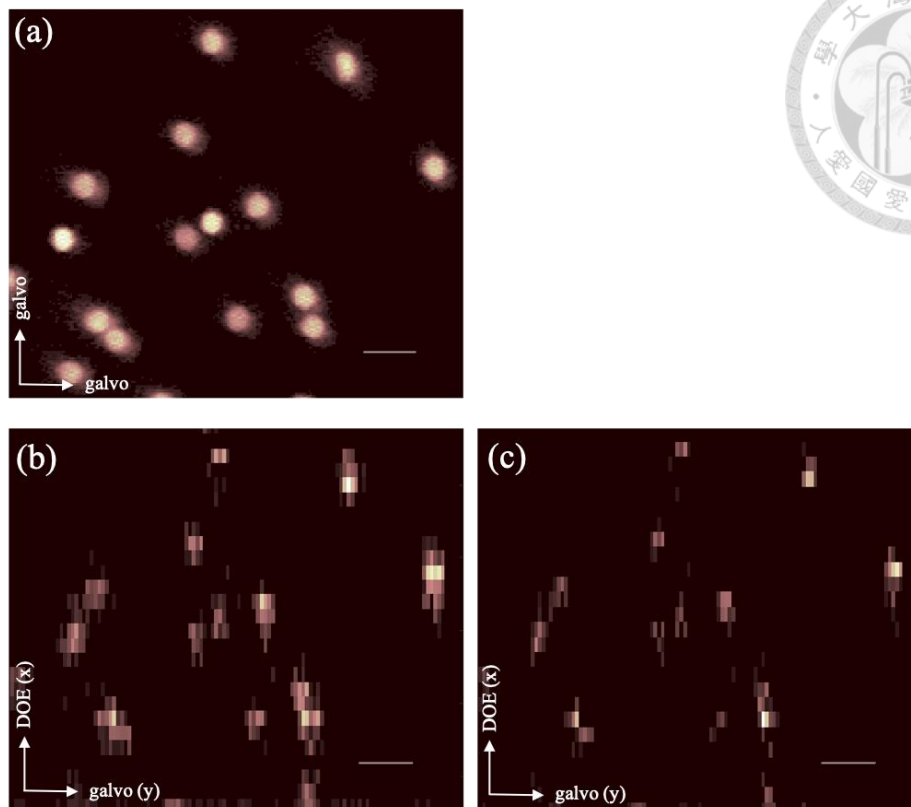
Fig. 4.1.1 Fluorescence microspheres before and after photon reassignment

(a) Slow scan image of 10 μm fluorescence microspheres acquired by single-beam and

a single-channel PMT. Scale bar, 30 μm. (b) Fast scan image of 10 μm fluorescence

microspheres before photon reassignment. (c) Photon reassignment of fast scan image.

4.2　Shift on galvo axis

As shown in Fig. 2.4.1, the galvanometric mirror scans in a period generates two volumes.

Since the scanning direction is totally opposite, by flipping the even images on the galvo

axis, we shall obtain a similar image compared to the odd images. However, there is a

shift on the galvo axis after flipping the images, which is about 15 pixels (Fig. 4.2.1).
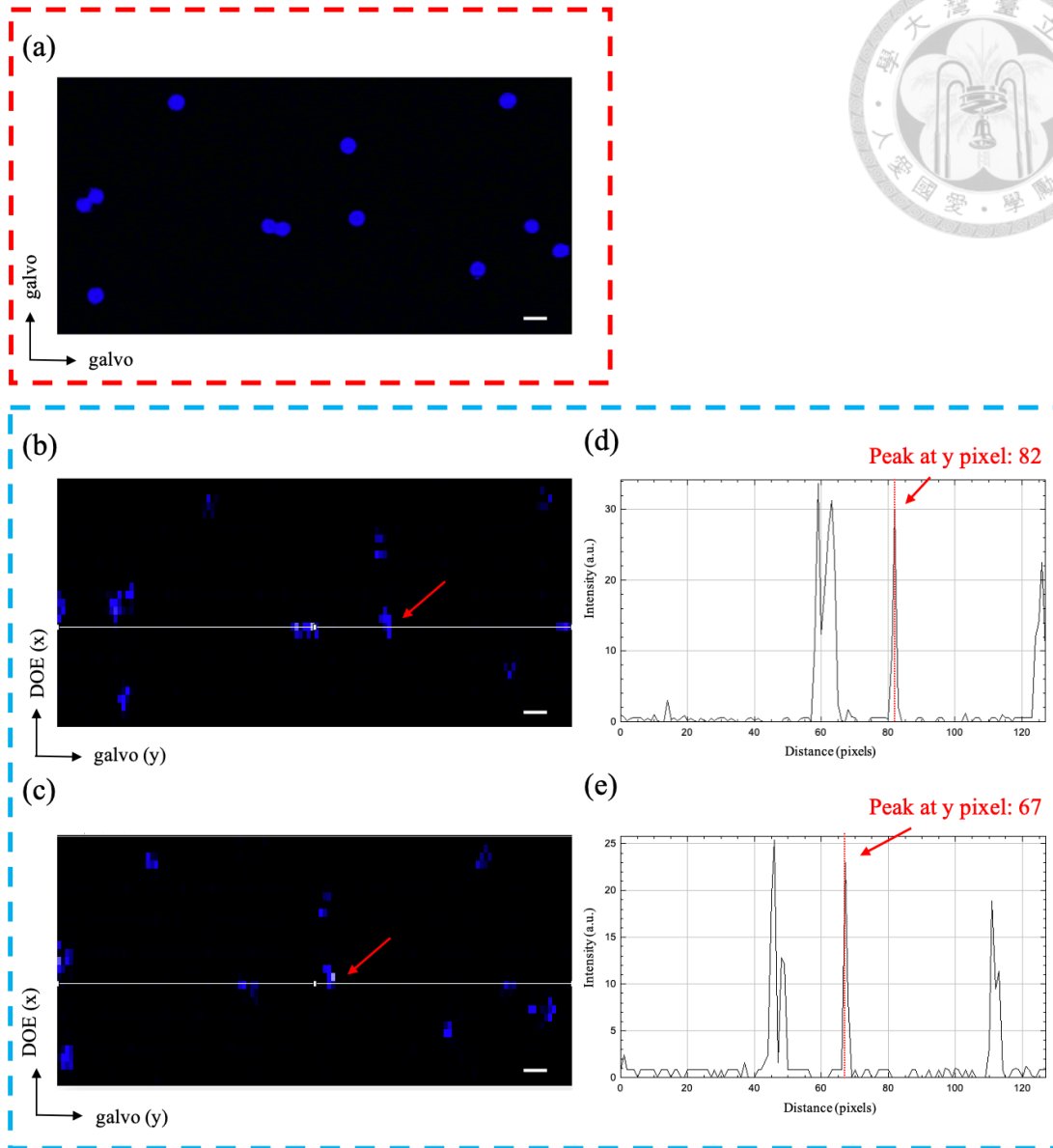
Fig. 4.2.1 Shift on galvo axis between odd and even volumes before phase changing

(a) Slow scan image of 10 μm fluorescence microspheres. (b-c) Same sample as (a) acquired by our high-speed microscope, corresponding to the odd and even (after flipping along y axis) volume image. Scale bar, 20 μm. (d-e) The line profile of the fluorescence signal (white line) that passes through the fluorescence microsphere, corresponding to (b) and (c). The red arrow indicates the microsphere and the y axis shift between the odd and even volume image is about 15 pixels.

The problem here is that the starting point on the galvo axis is incorrect. With one period (180 degrees) of galvanometric mirror corresponding to 256 pixels (2 × 128 pixels) in our system, 15 pixels correspond to ~ 10 degrees. With the help of our lab member Ting-Chen Chang by adding the parameter of "Phase Adjustment (degree)" on the control panel of the data acquisition software (Fig. 4.2.2). We are able to change the default starting phase from -90 degree to -80 degree for obtaining images without shifting (Fig. 4.2.3).
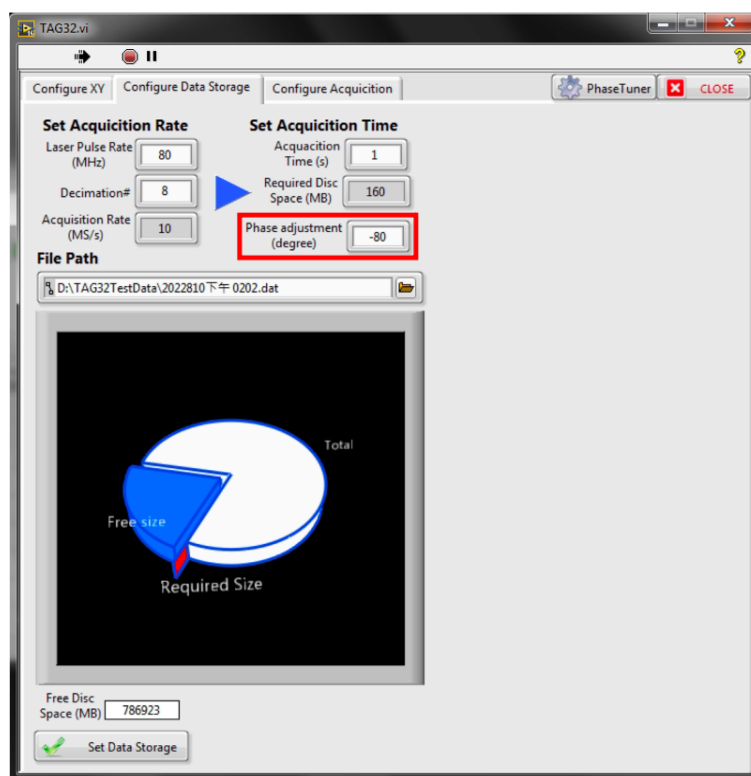
Fig. 4.2.2 Phase adjustment parameter on the data acquisition software control panel
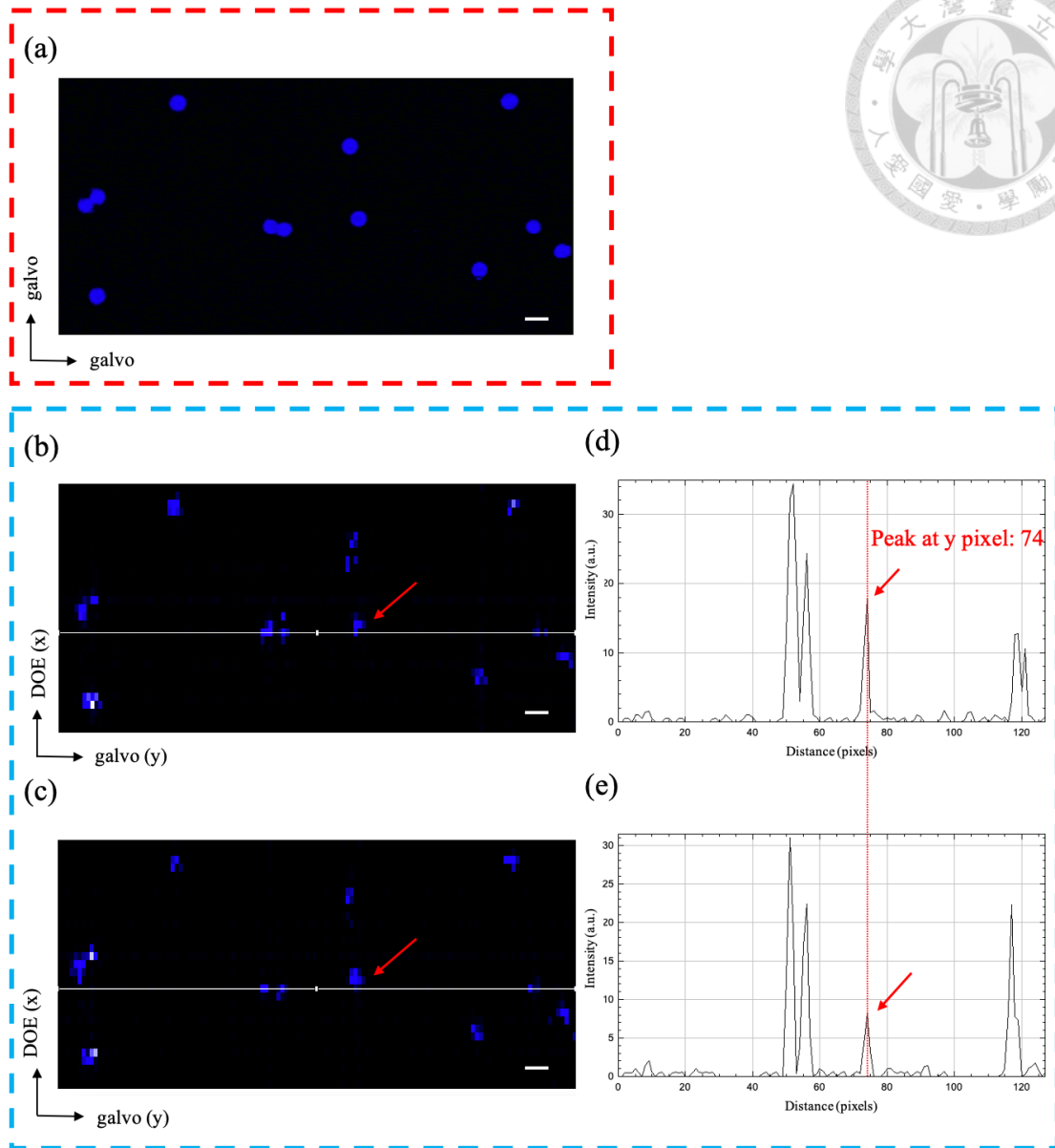
Fig. 4.2.3 Odd and even volumes after phase changing

(a) Slow scan image of 10 μm fluorescence microspheres. (b-c) 10 μm fluorescence microspheres acquired by our high-speed microscope, corresponding to the odd and even (after flipping along y axis) volume image. Scale bar, 20 μm. (d-e) The line profile of the fluorescence signal (white line) that passes through the fluorescence microsphere, corresponds to (b) and (c). The red arrow indicates the microsphere with no shift between odd and even images.

4.3 Missing data causing image shift
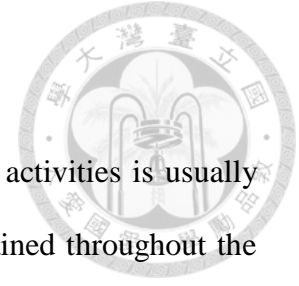
Since the time span in a biology experiment to observe functional activities is usually longer than several seconds. The imaging quality should be maintained throughout the imaging time. However, we have discovered a random shift on the galvo axis and z axis. The position of the fluorescence microspheres is shown in Fig. 4.3.1a via slow scan imaging. We then switch to fast scan imaging with acquisition time for more than 5 seconds. The image is normal in volume 2811 and 2812, correspondingly shown in Fig. 4.3.1b and Fig. 4.3.1c, but it suddenly changes in one volume, which is ~2 ms, as shown in Fig. 4.3.1d. The top image shows only a single layer and the bottom image shows the projection on xy-plane. This indicates the signals are shifted on both the y and z axis. The phenomenon might be caused by missing data, thus affecting the image reconstruction.
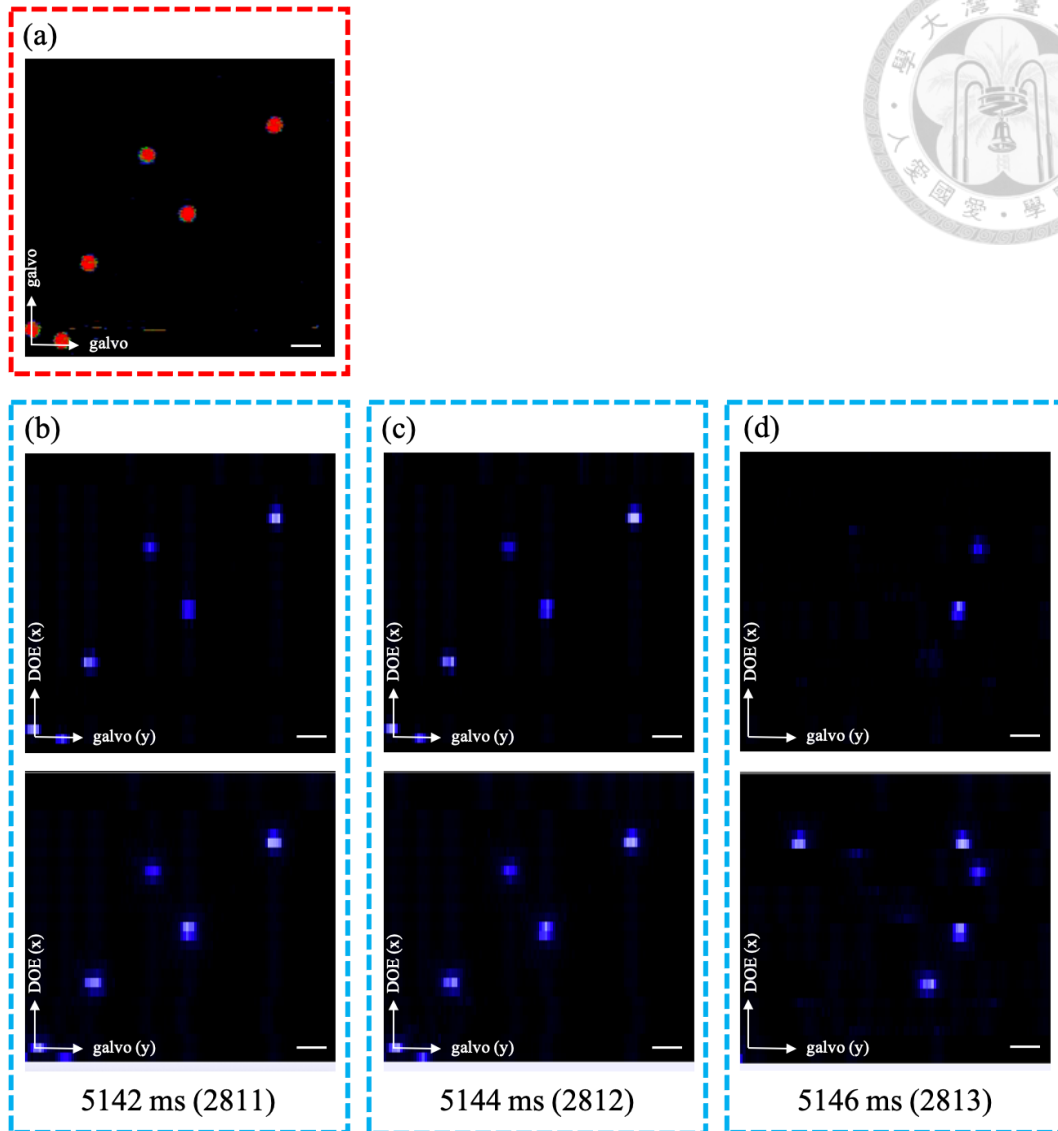
Fig. 4.3.1 Missing data causes fluorescence microspheres shift on y and z axis

(a) Slow scan image of 10 μm fluorescence microspheres. (b), (c), (d) 10 μm fluorescence microspheres acquired by our high-speed microscope, corresponding to the 2811th, 2812th and 2813th volumes. Top, single layer. Bottom, projection on xy-plane. Scale bar, 20 μm.

Here, we check the shifting pattern via the crosstalk induced by the fluorescence microspheres. As shown in Fig. 4.3.2, the signal shift happens every four channels, which correspond to an individual digitizer.
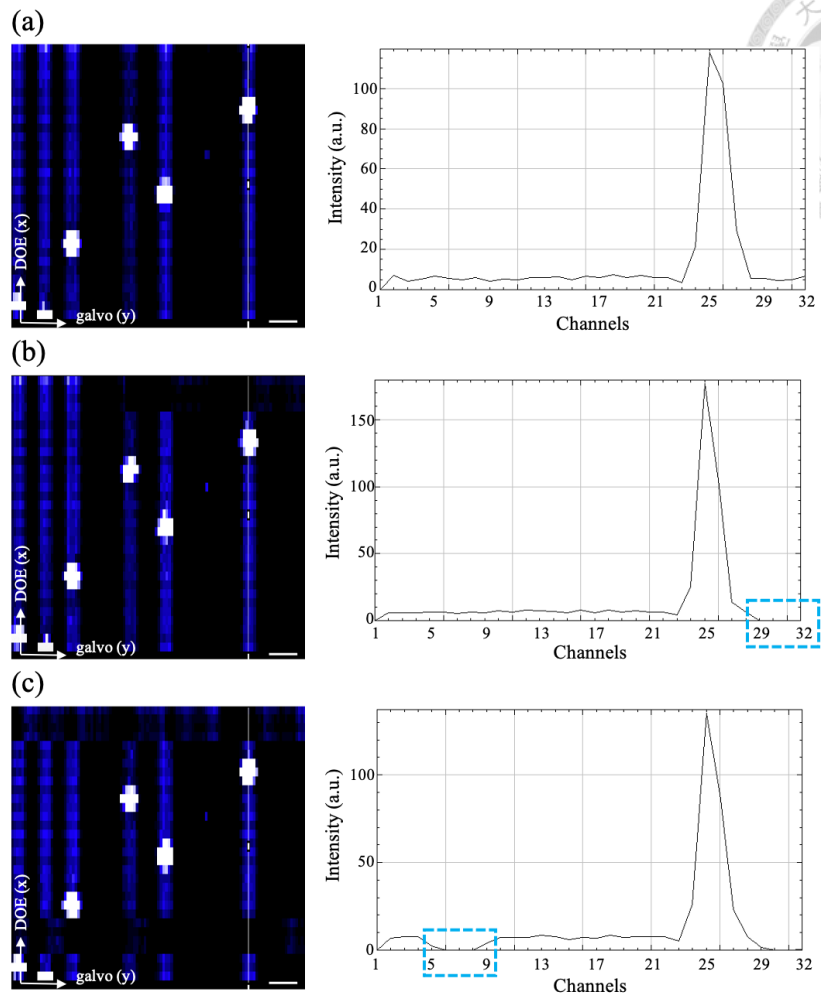
Fig. 4.3.2 Signal shift occurs in four channels

(a) Signal without shifting, the intensity of background is uniform. (b) Signal shift occurs at channel 29~32, which corresponds to the last digitizer. (c) Signal shift occurs at channel 5~8, which corresponds to the second digitizer.

Here, we test the TTL signal of the TAG lens, which might cause missing data on a single digitizer. The TTL signal is duplicated into eight signals via a printed circuit board (PCB) as shown in Fig. 4.3.3a. Those signals are then imported to the auxiliary I/O of the digitizer in order to synchronize the eight digitizers. If one specific TTL signal after the PCB is missing and is not synchronized with the original input TTL signal, the acquisition

time of the corresponding digitizer might be different from other digitizers, resulting in missing data and signal shifts.
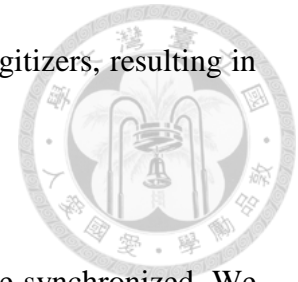
In order to confirm whether the TAG TTL signals after the PCB are synchronized. We duplicated the signals after the PCB via a T-joint connector and imported the signals into the analog input of the digitizer. By operating our data acquisition system, we are able to analyze the image pattern, and recognize whether the signals after the PCB are synchronized. Here, we import TAG TTL signals without passing through the PCB into channel 1, and import signal a~g which pass through the PCB into channel 2~8, sequentially (Fig. 4.3.3a). Since the TAG TTL signal is used for triggering the angle of the galvanometric mirror. The signals appear at the end of the period, which is the last few layers (128~142); in contrast, there are no signals on the rest of the layers. Fig. 4.3.3b shows volume 3451 (6332 ms) which presents the standard image, the top image is layer 16 and the bottom image is layer 130. However, at the next volume 3452 (6334 ms) as shown in Fig. 4.3.3c, the TTL signals which are imported into the second digitizer have shifted to the above layer (16). Since the TTL signals in charge of the second digitizer, which is imported to channel 3 (signal b, orange) still maintain at the last few layers, we are able to confirm the TTL signals are synchronized after the PCB.
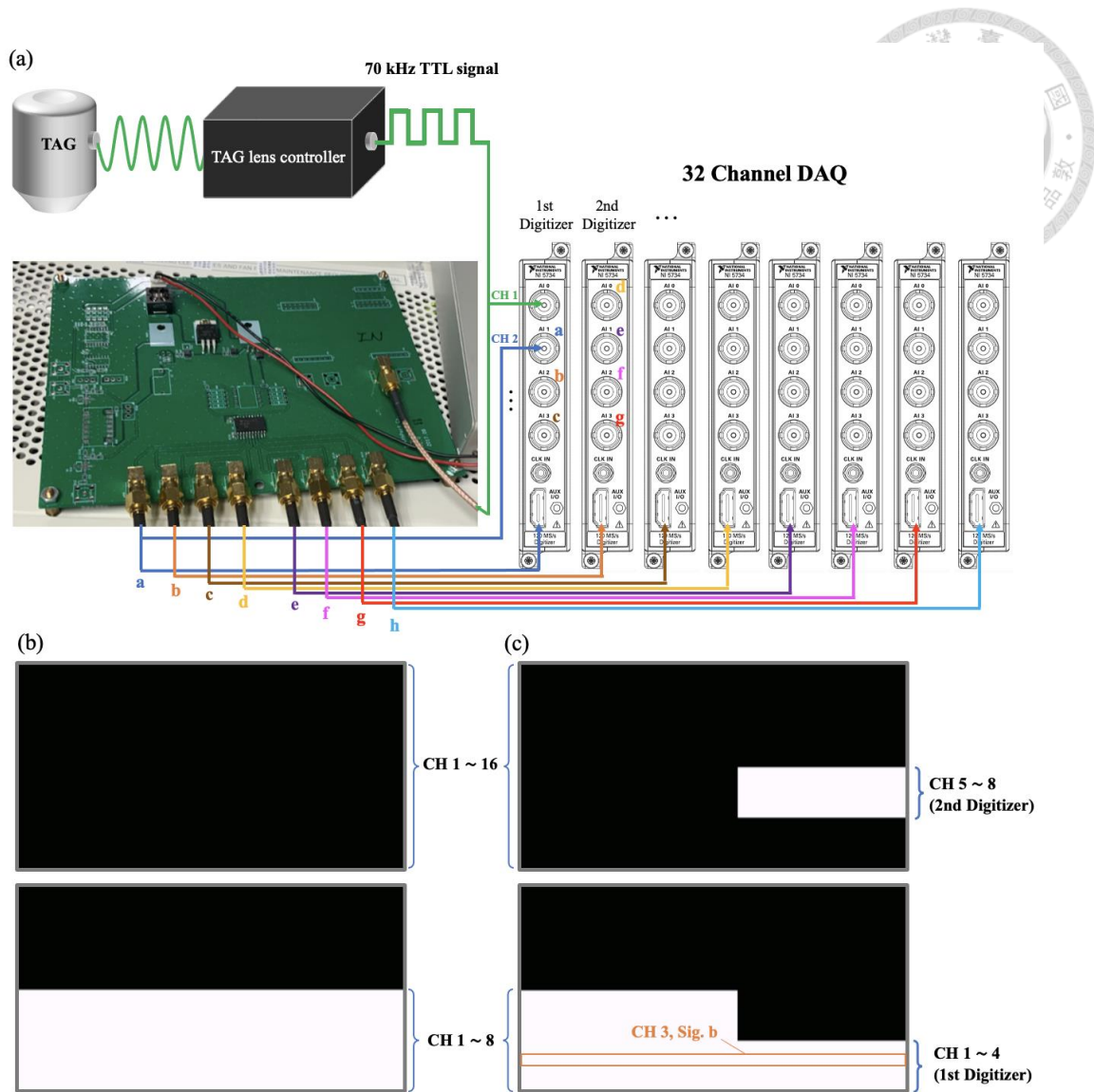
Fig. 4.3.3 Experiment of the synchronization of TAG signal after the PCB

(a) PCB of duplicating the TAG TTL signals to synchronize the eight digitizers. The

dualed signals are also imported into the analog input of the digitizer. (b-c) Acquired

image of volume 3451 (6332 ms) and 3452 (6334 ms). Top, layer 16 on z axis. Bottom,

layer 130 on z axis.

Chapter 5. Biology results
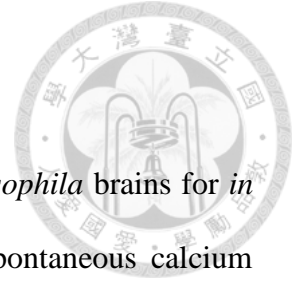
In this chapter, we apply our system on the GCaMP7f-labeled *Drosophila* brains for *in vivo* imaging. We then observe the functional image including spontaneous calcium dynamics and periodic activity in MB via electric stimulation.

5.1 Functional *Drosophila* imaging: Spontaneous

As mentioned in the previous section, missing data causes imaging shifts. Before analyzing the time-lapsed brain images, we need to check whether the image is shifted. In order to observe the MB of the *Drosophila*, we place the cuticle-removed fly under our high-speed microscopy and accumulate 100 acquired volume images. There are ~1100 volumes within 2s. Comparing first and last 100 volumes, as shown in Fig. 5.1.1a and Fig. 5.1.1b, the MB maintains at the same region, so we move on to analyzing the images temporally. This result also proved that our high-speed multi-beam microscope is able to acquire *in vivo Drosophila* brain image.
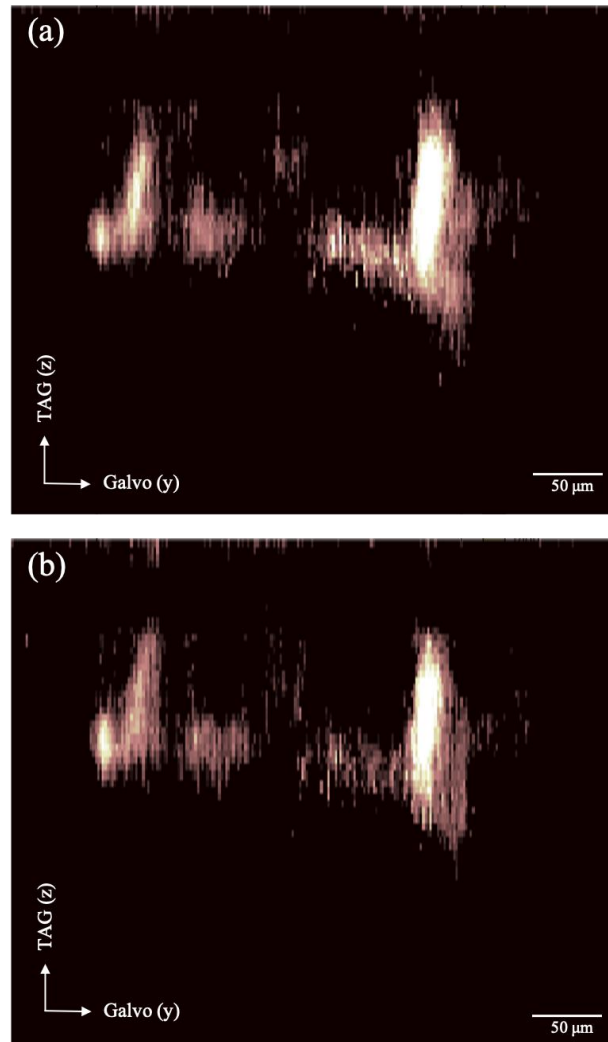
Fig. 5.1.1 Accumulating 100 volumes of fast scan images

(a) Accumulate the first 100 volumes of MB (1-100). (b) Accumulate the last 100

volumes of MB (1000-1100). Scale bar 50 μm.

After confirming the images are not shifted, we analyze the calcium-dependent

fluorescence changes ($\Delta F/F_0$) inside the MB, which is the central processing unit of a

Drosophila. Fig. 5.1.2a is the anatomical structure of the MB with three subcompartments

in the alpha lobes. With the slow scan imaging, we are able to acquire a 2D image (xy-

plane) of the MB (orange) inside the *Drosophila* head capsule (purple), as shown in Fig.

5.1.2b. After switching to our high-speed multifocus microscope, and accumulating 100

volumes (~ 180 ms) and projection on the yz-plane, we clearly see the left and right alpha

60

lobes of MB, as shown in Fig. 5.1.2c. In order to resolve the calcium dynamics in a living MB lobe, we observe the axially resolved signal of the right MB, as marked by the white boxes in Fig. 5.1.2c. Each box is $25 \times 17 \times 5$ μm^3, corresponding to $4 \times 10 \times 1$ pixels in x, y, and z axis, respectively. The spatiotemporally resolved $\Delta F/F_0$ signals of the boxes are presented in Fig. 5.1.2d (gaussian smoothing, window size = 366 ms). This figure presents the different intensity in the subcompartments of the right lobe of MB, where R1, R2 and R3 correspond to Fig. 5.1.2a. The colored arrow indicates the different $\Delta F/F_0$ peak of the subcompartments. With repeating the same experiments on different *Drosophila*, as shown in Fig. 5.1.3, the spatiotemporal results reveal a distinct transient response in R3, which corresponds to the subcompartment in Fig. 5.1.2a. The projection in the top of Fig. 5.1.3c shows the distinct response in R3 (black arrow) through highlighting the fluctuation from the average of normalized responses. In the next section, in order to achieve a much more obvious calcium dynamic, we stimulate the *Drosophila* to acquire a periodic response inside the MB.
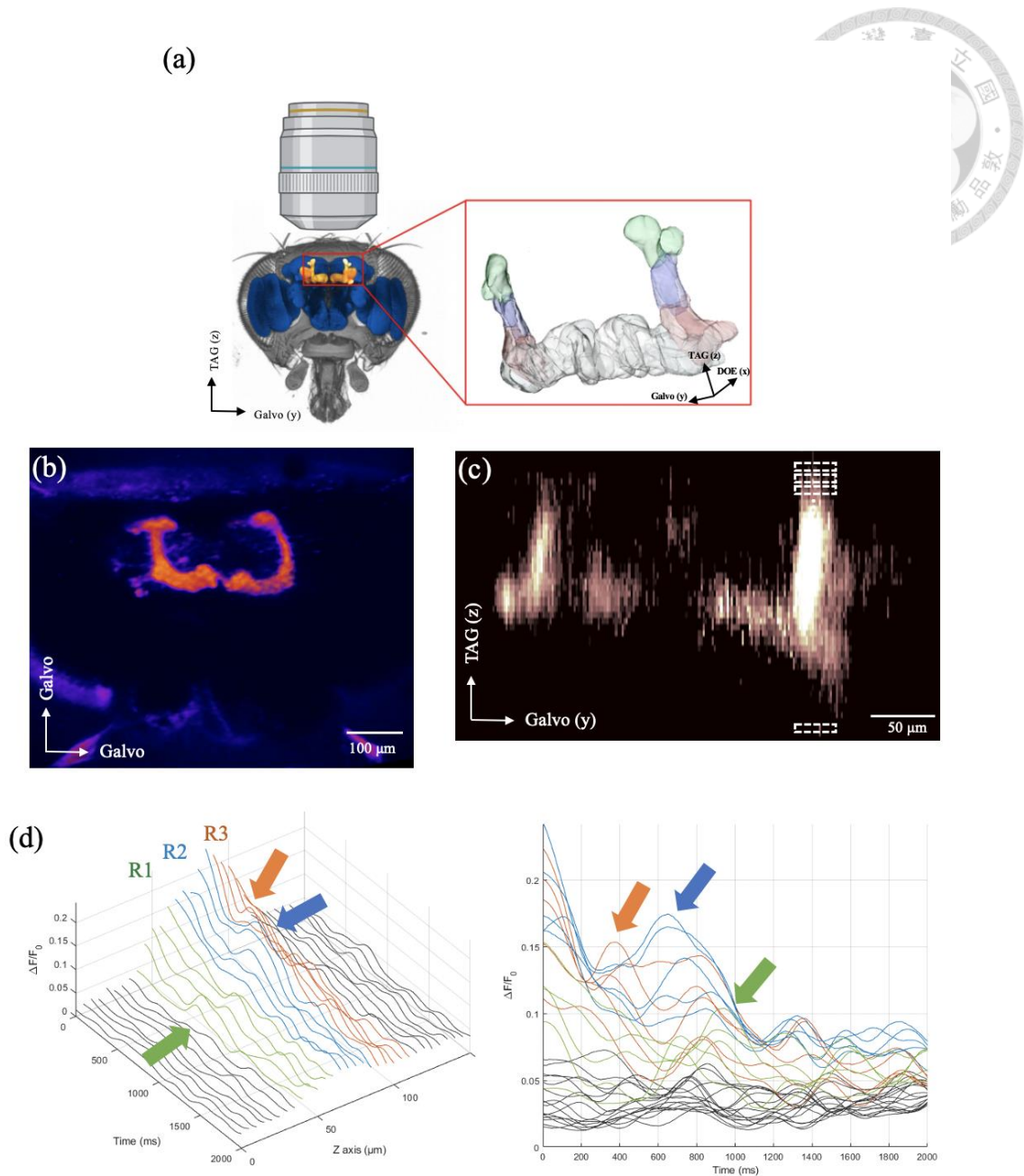
Fig. 5.1.2 *Drosophila* brain image and spontaneous fluorescence changes in MB

(a) Mushroom body inside a *Drosophila* brain. Inset, three subcompartments (colors) in

the alpha lobes. (b) *In vivo* observation of MB labeled with GCaMP7f by slow scan.

Purple, *Drosophila* head capsule. Orange, MB. Scale bar, 100 μm. (c) Structure of the

MB captured by high-speed microscopy (accumulates 100 volumes) projected to the yz-

plane (y, galvanometric axis; z, TAG axis). Scale bar, 50 μm. (d) The $\Delta F/F_0$ of the right

alpha lobe of MB cross section along z direction, each line corresponds to each white

box in (c). Three colors relate to the three subcompartments in (a).

(a)

(b)

(c)
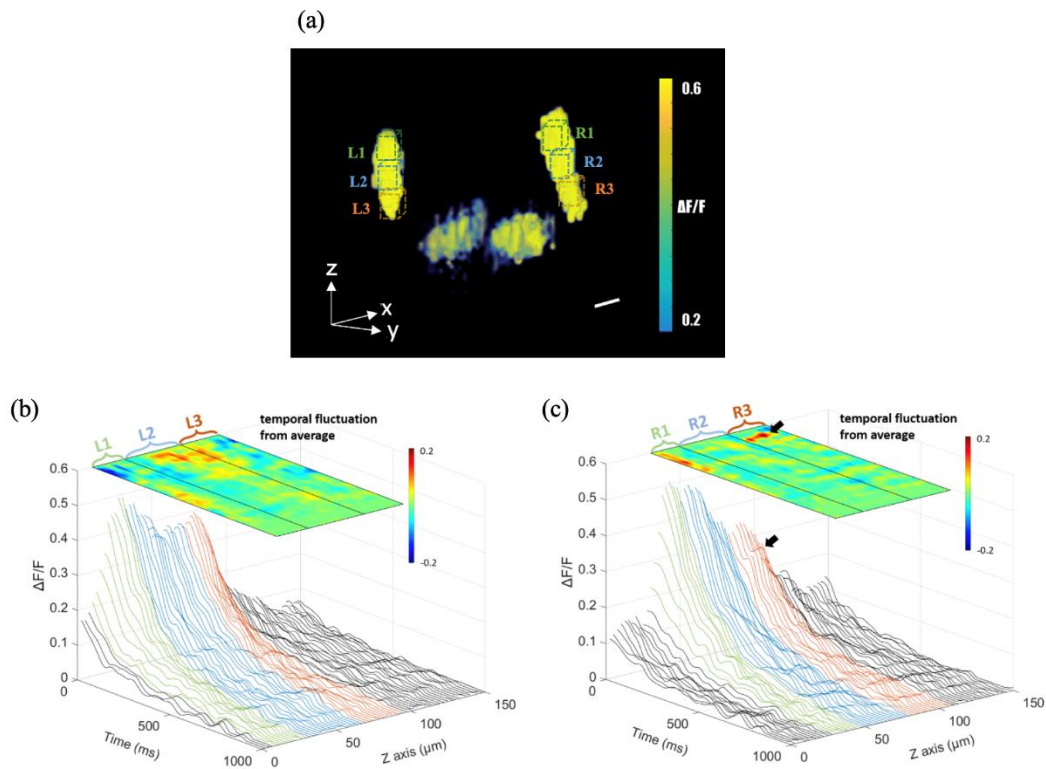
Fig. 5.1.3 Time-lapsed images of MB and fluorescence changes in the alpha lobes

(a) Fast scan MB time-lapsed volumetric images. Scale bar, 50 μm. (Link: https://drive.

google.com/file/d/1KKKKPciyRC2m5by76qmvf1sFAxcRpr17/view?usp=sharing)

(b-c) $\Delta F/F_0$ of the left and right lobe. The black arrow indicates the distinct transient

response in R3. Notice that the intensity decay is the heat absorption caused by the TAG

lens which will be mentioned at section 6.3, this causes the image intensity decreases.

By highlighting the fluctuation from the average of normalized responses, the distinct

response in R3 (black arrow) is shown at the projection in the top of (c).

5.2 Functional *Drosophila* imaging: Electric simulation

In order to carry out periodic functional imaging in *Drosophila*, there are several ways to

stimulate the fly, for example light, odor, and electric shocks. Here, we use electric shocks

for stimulation, since it fires most of the neurons inside the brain. As mentioned in section

3.3.4, we applied 25V stimulation for 0.7s, and relaxed for 1 s. (Fig. 5.2.1).

63
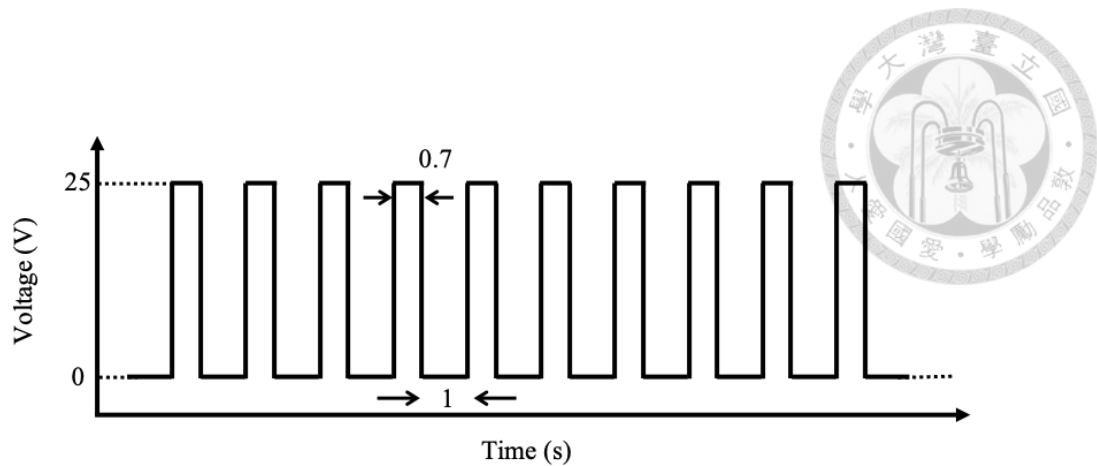
Fig. 5.2.1 Electric stimulation

Before high-speed imaging, we utilize slow scan to observe the structure of the MB (Fig. 5.2.2a), the volume image is achieved by changing the height of the z-stage (GSC-01, OptoSigma). In order to confirm whether the MB is stimulated, we zoom in the alpha lobe of the MB and stimulate the *Drosophila*. With the frame rate of ~164 ms (128 × 128 pixels, 10 µs pixel dwell time), we capture 2D time-lapsed images (Fig. 5.2.2b). The time series of $\Delta F/F_0$ changes with 1.7 s periodicity (Fig. 5.2.2c), also after utilizing the Fourier transform, the peak shown in frequency domain is around 0.58 Hz (Fig. 5.2.2d), which matches our electrical period. Thus, this verifies the MB is stimulated by the electric shocks.
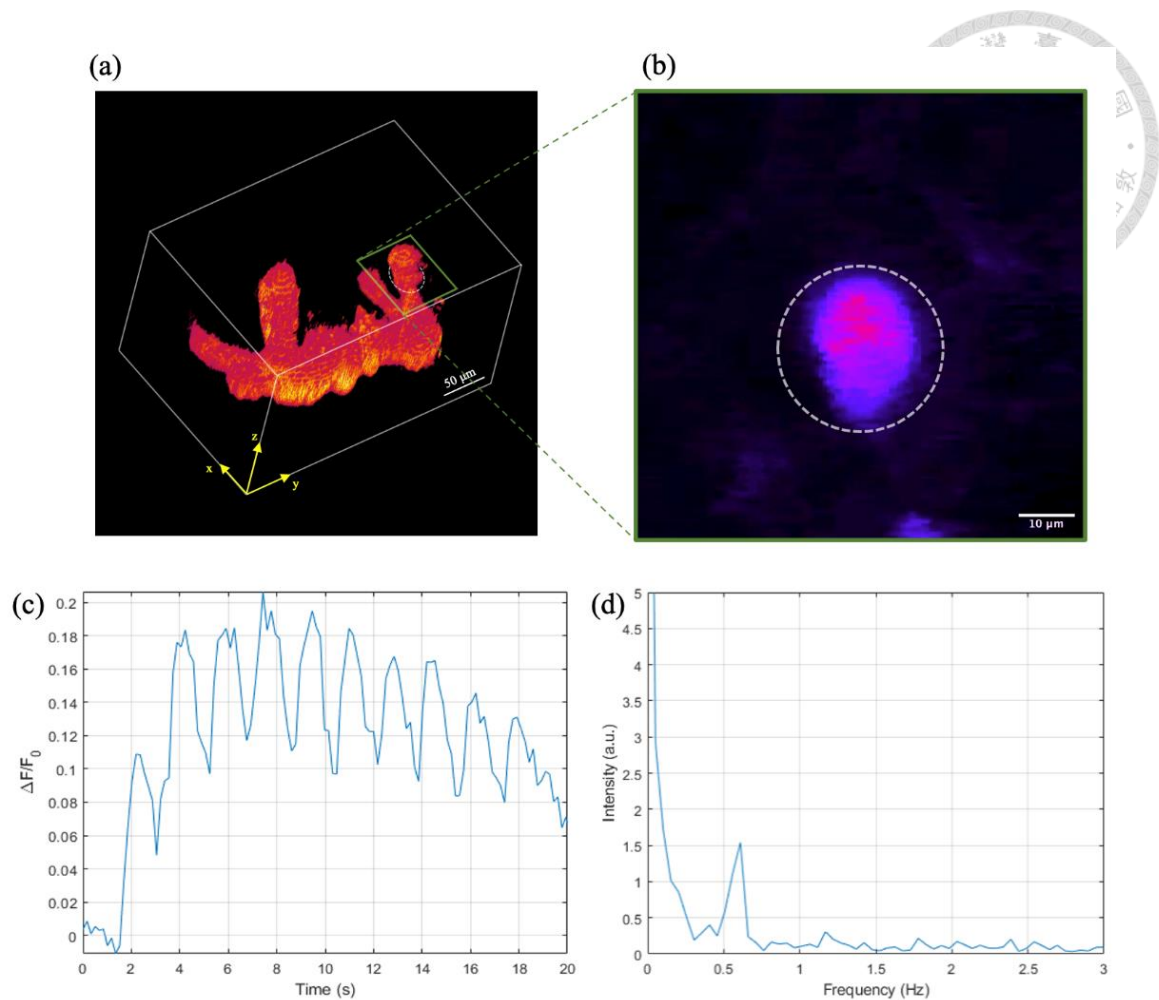
Fig. 5.2.2 Slow scan image stack and the fluorescence intensity change

(a) Slow scan image of the 3D structure of MB by the movement of the z-stage. Scale

bar, 50 μm. (b) Zoom in the right alpha lobe of the MB (green area) to achieve 2D time-

lapsed images. Scale bar, 10 μm. (Link: https://drive.google.com/file/d/1ovbxlAGpMZ

076evot5N3_ImicA73Jgrn/view?usp=sharing) (c-d) Time and frequency domain of

$\Delta F/F_0$ in the area of the right alpha lobe marked by white circle.

After confirming the MB is successfully stimulated by the electric shock, we switch to

our high-speed microscope to achieve millisecond scale volumetric image and stimulate

the *Drosophila* with the same protocol. There are 3000 volumes within 5500 ms. By

accumulating 200 volumes (~ 366 ms) and projection on the yz-plane, we repeat the

analysis in section 5.1. The region of interest is marked by the white box in Fig. 5.2.3a.

65
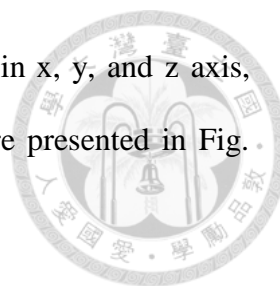
Each box is $25 \times 16.4 \times 5\ \mu m^3$, corresponding to $4 \times 6 \times 1$ pixels in x, y, and z axis, respectively. The spatiotemporally resolved signals of the boxes are presented in Fig. 5.2.3b (gaussian smoothing, window size = 366 ms).
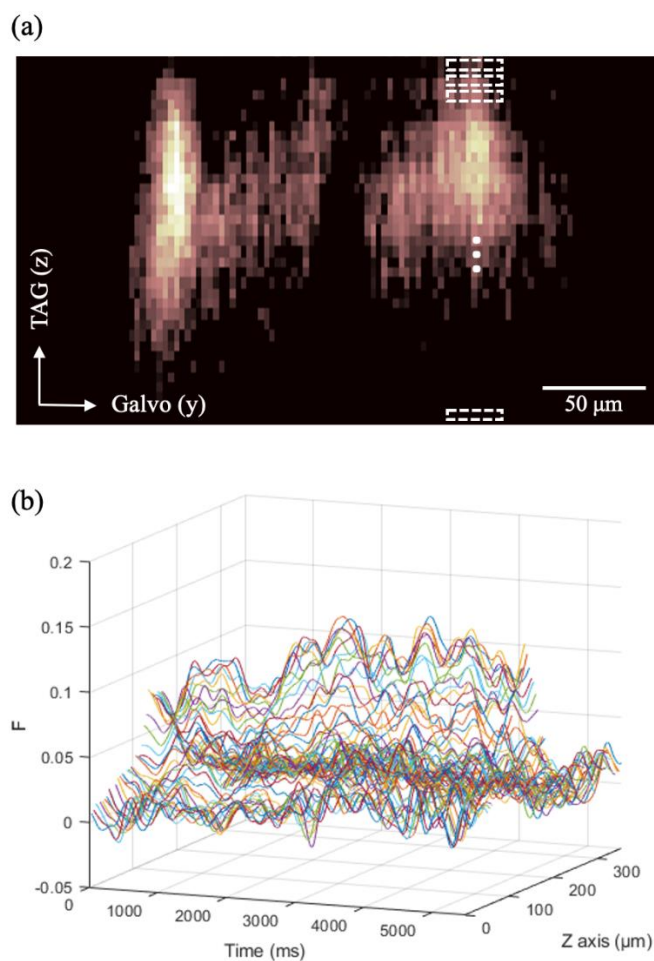
Fig. 5.2.3 Fast-scan imaging of MB and the multilayer fluorescence intensity

(a) Structure of the MB captured by multibeam and multichannel PMT (accumulate 200 volumes) projected to the yz-plane (y, galvanometric axis; z, TAG axis). Scale bar, 50 μm. (b) The signal intensity of the right MB cross section along z direction, each white box in (a) corresponds to each line.

In order to confirm the frequency of the calcium dynamics signal is the same as the stimulation frequency, we analyze each layer inside and outside the right lobe of MB, which is our treatment and control group. Fig. 5.2.4a indicates the area inside and outside

66

the MB, which is the blue and red area, respectively. We select the layers inside the areas and show the fluorescence intensity changes spatiotemporally in Fig. 5.2.4b and Fig. 5.2.4c, which corresponds to the treatment and control group (gaussian smoothing, window size = 366 ms). The top and bottom figures are viewed at different angles. After utilizing the Fourier transform of each layer inside the MB (treatment group), there is a peak at around 0.58 Hz (Fig. 5.2.5a), which corresponds to our electrical stimulation. On the other hand, with the Fourier transform of the control group, there is no peak around 0.58 Hz (Fig. 5.2.5b). Utilizing a bandpass filter with passband frequencies of 0.2 Hz and 1.2 Hz, the filtered signal is shown in Fig. 5.2.5c and Fig. 5.2.5d. Where the three periods in the time domain are clearer in the experiment group than in the control group. This shows the MB area is stimulated by electric shock and is able to be observed through our high-speed microscope.
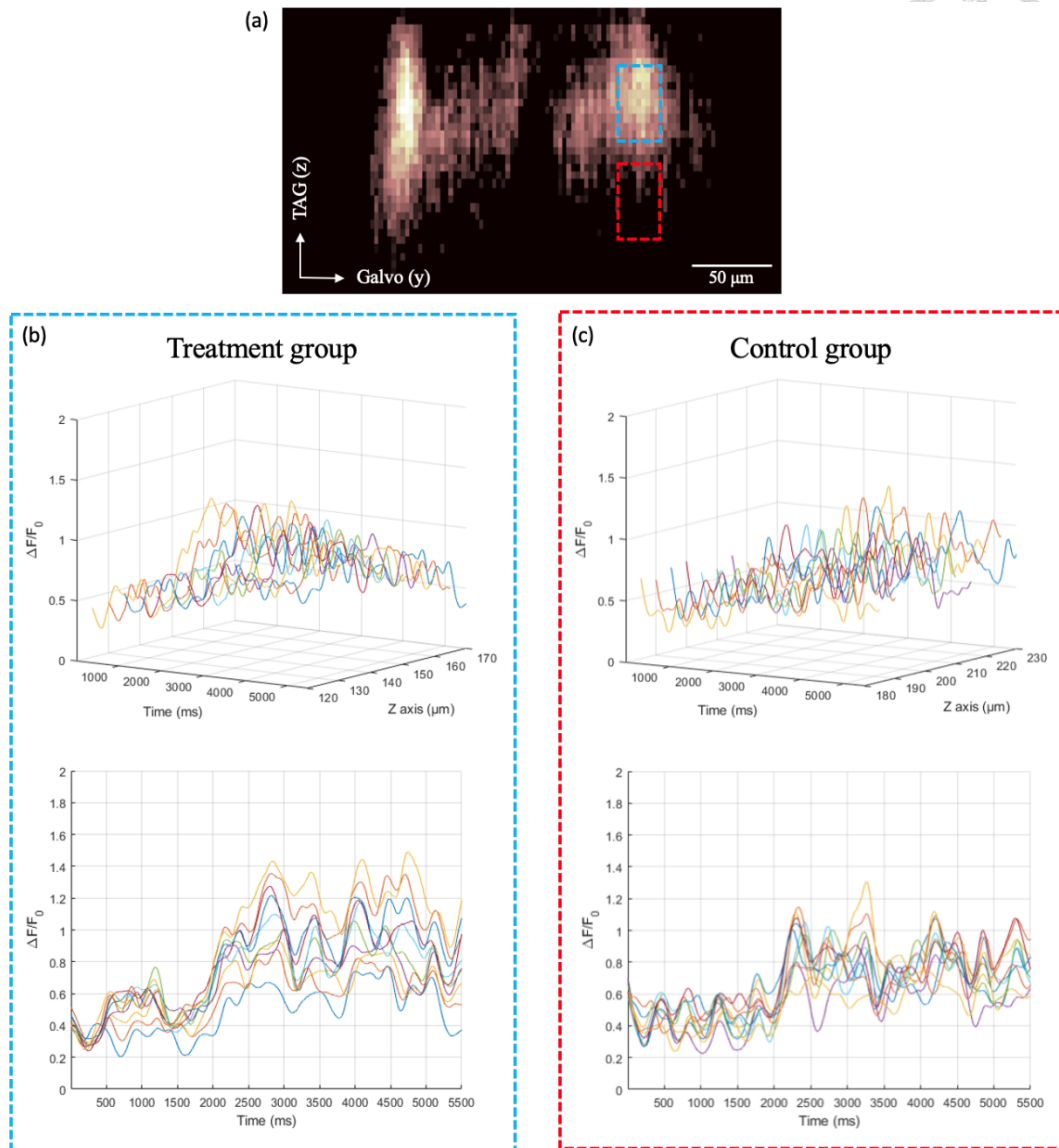
Fig. 5.2.4 The spatiotemporal ΔF/F$_0$ inside and outside the MB

(a) The areas inside (blue) and outside (red) the right lobe of MB corresponds to our treatment and control group. Scale bar, 50 μm. (b-c) The ΔF/F$_0$ calcium dynamics signal of the multiple layers inside the MB (blue area) and outside the MB (red area). Top, 3D presentation. Bottom, projection along the z axis.
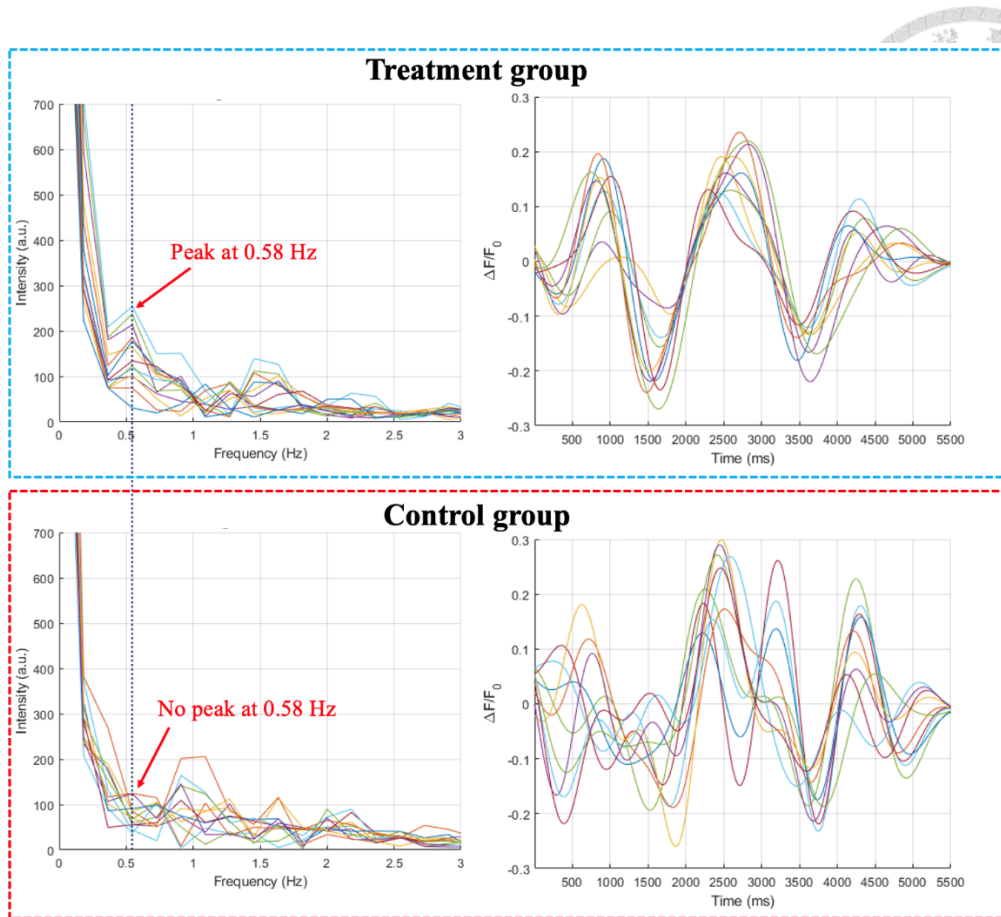
Fig. 5.2.5 Fourier transform and the filtered signal of the MB area and control group
(a-b) Frequency domain of the $\Delta F/F_0$ inside the MB area (blue) and the control group
(red). (c-d) Time domain of the filtered signal. Specify passband frequencies of 0.2 Hz
and 1.2 Hz.

Chapter 6. Conclusion and discussion
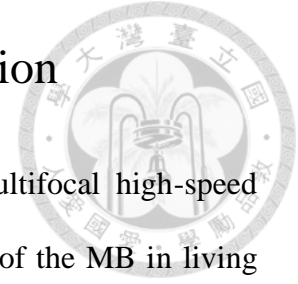
In conclusion, we combined DOE and TAG lens to achieve multifocal high-speed microscopy, with observing spontaneous and stimulation response of the MB in living *Drosophila*. My contribution in this study is to confirm that our high-speed multifocal two-photon microscopy is able to achieve *in vivo Drosophila* functional brain imaging and the missing data testing with TAG TTL synchronization. Our high-speed system sacrifices the step size (6 μm, 3.5 μm and 5 μm in x, y and z axis, respectively) to achieve high temporal resolution with 2 ms. However, the emitted photon yield per pulse is only ~3 photons/pulse, which is the ideal number for low-scattering tissue. Since our sample, *in vivo Drosophila*, is a high-scattering tissue, one volumetric image is too dark to resolve a single neuron. Thus, to observe the structure image, we accumulate the images temporally to enhance the fluorescent signals, this results in decreasing the imaging speed, as shown in Fig. 5.1.1. In order to observe the functional response, we spatially average the signals along the MB cross section, as shown in Fig. 5.1.2c, resulting in decreasing the spatial resolution.

6.1 Increasing the emitted photon yield

In order to increase the emitted photon yield per pulse, we are able to optimize the excitation and emission portion. For excitation, we utilize an 80 MHz repetition rate laser, which is often used for 2PM. However, the repetition rate is too high for our experiment because of this over-sampling on the z axis (~570 pixels along 360 μm, z resolution: ~5.5 μm), so here we average eight pixels into one pixel as we mentioned in section 3.2. Nevertheless, recent study has shown that the ideal repetition rate for deep tissue 2PM is 1~10 MHz repetition rate [72]. In the future, we are going to utilize a 10 MHz laser by

adding eight laser pulses into one pulse, resulting in an eight-fold increase in the peak power of the laser pulse. The emitted photon yield per pulse elevates 64 times (8^2 times), due to the nonlinearity of two-photon excitation.

For emission, the detecting system we use is a descanned system, as shown in Fig. 3.1.1. The fluorescent beams are maintained at the same position on the detector while the galvanometric mirror is scanning. However, the scattering photons are not able to reach the detector due to the long light path, resulting in low signal intensity, especially in high-scattering tissue [34]. In the future, we consider a non-descanned system, which shortens the light path between the sample and the detector. The difficulty is to separate the multibeam to match the corresponding multichannel PMT while focusing the beams scanning in the PMT detecting area. The optimization on the excitation and emission portion is able to increase the emitted photon yield per pulse, resulting in higher signal intensity.

6.2 CPU performance might cause missing data

As mentioned in section 4.3, the missing data is still not solved, with the experiments done by our lab members Ting-Chen Chang and Chung-Ming Chen, the possible reason for the missing data might be the software-induced low CPU processing efficiency. Since we have proved that the TAG TTL signals after the PCB are synchronized, we are able to observe the signal shifts via importing those signals into the analog input of the digitizer. As shown in Fig. 6.2.1a, the TAG TTL signal without passing through the PCB is imported into the first digitizer (channel 1), signal b and c are imported into the second and third digitizer (channel 5 and channel 9), respectively. With CPU stress testing, we notice that the signal shifts occur at high CPU stress (Fig.6.2.1b-c). By changing to a higher performance CPU, this problem might be solved.

71
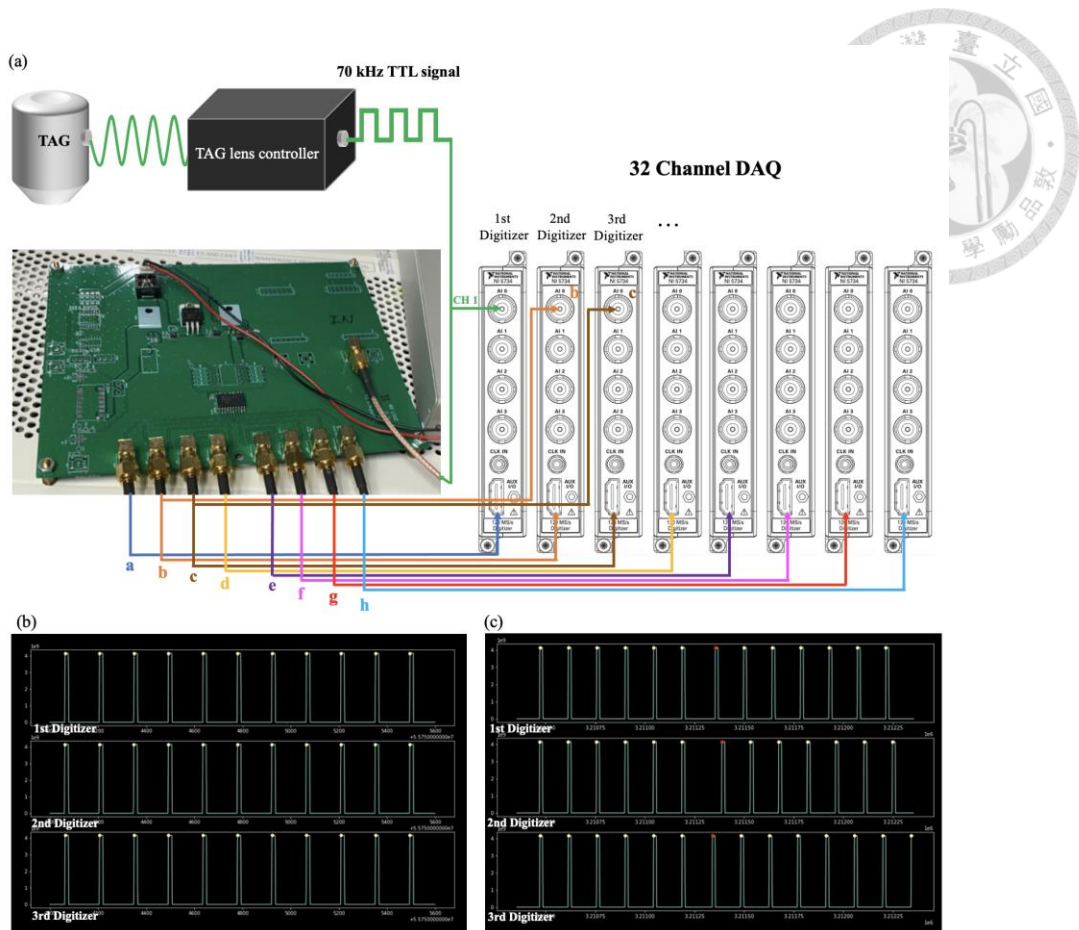
Fig. 6.2.1 CPU stress experiment

(a) The TAG TTL signal layout of testing CPU stress. (b) The TTL signals are not shifting at low CPU stress. (c) The TTL signals shift at high CPU stress (red spots).

6.3 Absorption of the TAG lens

Although the TAG lens offers high-speed axial scanning, our previous lab member Yu-Hsuan Tsai found with large incident power (~500 mW) on the TAG lens, it causes thermal-induced aberration due to non-uniform heating of the silicone oil inside the TAG lens. Thus, this might change the laser wavefront after the TAG lens, resulting in intensity decreases over time. As shown in Fig. 6.3.1a and Fig. 6.3.1b, which is the image of a portion of 32 foci captured by sCMOS utilizing FITC solution, the intensity is lower after the thermal effect of the TAG lens (3 sec) compared to the thermal effect occurs (0 sec). Fig. 6.3.1c presents the intensity decay in three seconds, which is similar to Fig. 5.1.3.

72

With low incident power, we are able to avoid this heat absorption. Another possible way is to change a TAG lens which has low-power absorption material, this depends on whether the TAG lens company offers such kind of commercial TAG lens.
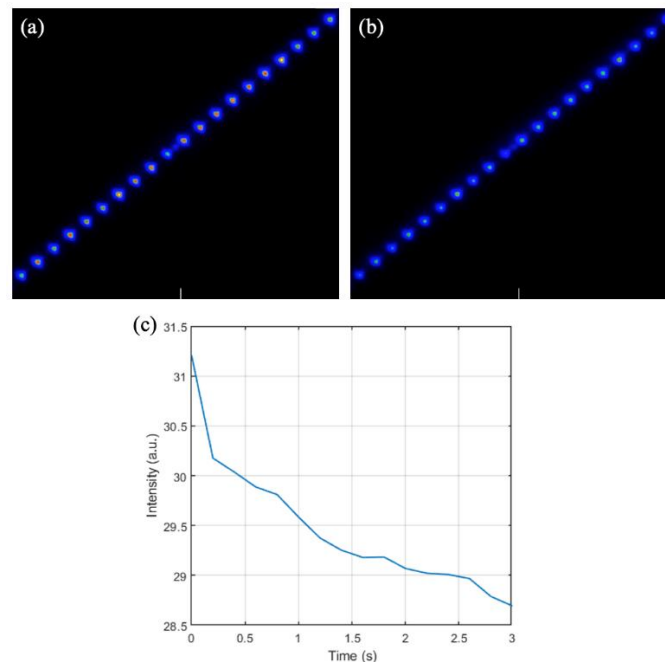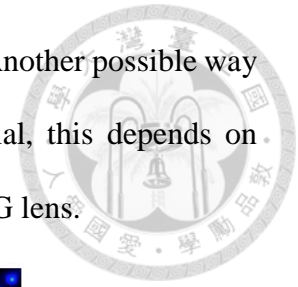
Fig. 6.3.1 32 foci under TAG lens thermal effect

(a) Before the TAG lens induced thermal effect (0 sec). (b) After the TAG lens thermal effect (3 sec). (c) The intensity of the foci decreases due to the thermal effect.
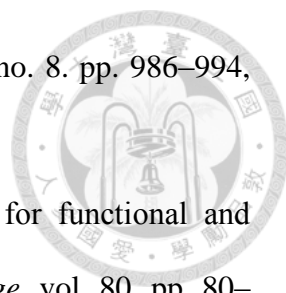
6.4 Other applications of this system
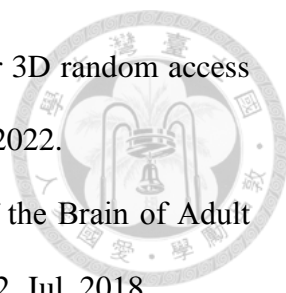
Although our microscopy is designed for the *Drosophila* brain, this high-speed imaging is able to observe volumetric cellular structure screening, for example blood cells in vessels. We mimic the cells moving at high speed by moving the fluorescent microsphere. (Link: https://drive.google.com/file/d/1PVnXxZKiUvYF6Co_e17pIMDd3R4OpXkV/view?usp=sharing) Since our microscopy scanned the z axis via the TAG lens operating with a high-speed, this made our microscopy work like a vertical light sheet, which is perfect for vertical structure such as Purkinje cells in mice brain [73]. These applications might be possible ways to push forward in the future.
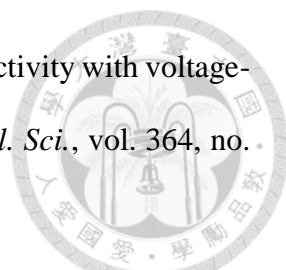
REFERENCE
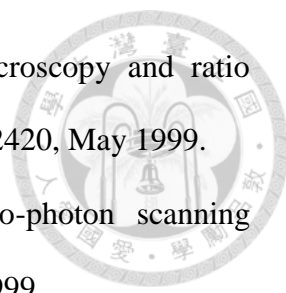
[1] C. Seife, "So much more to know," *Science*, vol. 309, no. 5731, pp. 78–102, Jul. 2005.

[2] M. Glickstein, "Golgi and Cajal: The neuron doctrine and the 100th anniversary of the 1906 Nobel Prize," *Curr. Biol.*, vol. 16, no. 5, pp. R147–51, Mar. 2006.

[3] M. F. Bear, B. W. Connors, and M. A. Paradiso, *Neuroscience: Exploring the Brain*. Lippincott Williams & Wilkins, 1996.

[4] D. Schubert, R. Kötter, H. J. Luhmann, and J. F. Staiger, "Morphology, electrophysiology and functional input connectivity of pyramidal neurons characterizes a genuine layer va in the primary somatosensory cortex," *Cereb. Cortex*, vol. 16, no. 2, pp. 223–236, Feb. 2006.

[5] F. Li *et al.*, "The connectome of the adult Drosophila mushroom body provides insights into function," *Elife*, vol. 9, Dec. 2020.

[6] Z. Zhang, L. Cong, L. Bai, and K. Wang, "Light-field microscopy for fast volumetric brain imaging," *J. Neurosci. Methods*, vol. 352, p. 109083, Mar. 2021.

[7] N. J. Butcher, A. B. Friedrich, Z. Lu, H. Tanimoto, and I. A. Meinertzhagen, "Different classes of input and output neurons reveal new features in microglomeruli of the adult Drosophila mushroom body calyx," *J. Comp. Neurol.*, vol. 520, no. 10, pp. 2185–2201, Jul. 2012.

[8] S. Weisenburger and A. Vaziri, "A Guide to Emerging Technologies for Large-Scale and Whole-Brain Optical Imaging of Neuronal Activity," *Annu. Rev. Neurosci.*, vol. 41, pp. 431–452, Jul. 2018.

[9] M. Uecker, S. Zhang, D. Voit, A. Karaus, K.-D. Merboldt, and J. Frahm, "Real-time

MRI at a resolution of 20 ms," *NMR in Biomedicine*, vol. 23, no. 8. pp. 986–994, 2010.

[10] K. Uğurbil *et al.*, "Pushing spatial and temporal resolution for functional and diffusion MRI in the Human Connectome Project," *Neuroimage*, vol. 80, pp. 80–104, Oct. 2013.

[11] N. M. Gage and B. Baars, "Fundamentals of Cognitive Neuroscience: A Beginner's Guide." *Academic Press*, 2018.

[12] N. Ji, J. Freeman, and S. L. Smith, "Technologies for imaging neural activity in large volumes," *Nat. Neurosci.*, vol. 19, no. 9, pp. 1154–1164, Aug. 2016.

[13] S. F. Cogan, "Neural stimulation and recording electrodes," *Annu. Rev. Biomed. Eng.*, vol. 10, pp. 275–309, 2008.

[14] B. A. Wilt, L. D. Burns, E. T. W. Ho, K. K. Ghosh, E. A. Mukamel, and M. J. Schnitzer, "Advances in Light Microscopy for Neuroscience," *Annual Review of Neuroscience*, vol. 32, no. 1. pp. 435–506, 2009.

[15] S.-H. Huang *et al.*, "Optical volumetric brain imaging: speed, depth, and resolution enhancement," *J. Phys. D Appl. Phys.*, vol. 54, no. 32, p. 323002, Jun. 2021.

[16] F. A. C. Azevedo *et al.*, "Equal numbers of neuronal and nonneuronal cells make the human brain an isometrically scaled-up primate brain," *The Journal of Comparative Neurology*, vol. 513, no. 5. pp. 532–541, 2009.

[17] H. Lv *et al.*, "Resting-State Functional MRI: Everything That Nonexperts Have Always Wanted to Know," *AJNR Am. J. Neuroradiol.*, vol. 39, no. 8, pp. 1390–1399, Aug. 2018.

[18] L. Squire, D. Berg, F. E. Bloom, S. du Lac, A. Ghosh, and N. C. Spitzer, *Fundamental Neuroscience*. Academic Press, 2013.

[19] F. K. Janiak *et al.*, "Non-telecentric two-photon microscopy for 3D random access mesoscale imaging," *Nat. Commun.*, vol. 13, no. 1, p. 544, Jan. 2022.

[20] Z. Zheng *et al.*, "A Complete Electron Microscopy Volume of the Brain of Adult Drosophila melanogaster," *Cell*, vol. 174, no. 3, pp. 730–743.e22, Jul. 2018.

[21] H. J. Bellen, C. Tong, and H. Tsuda, "100 years of Drosophila research and its impact on vertebrate neuroscience: a history lesson for the future," *Nat. Rev. Neurosci.*, vol. 11, no. 7, pp. 514–522, Jul. 2010.

[22] A.-S. Chiang *et al.*, "Three-dimensional reconstruction of brain-wide wiring networks in Drosophila at single-cell resolution," *Curr. Biol.*, vol. 21, no. 1, pp. 1–11, Jan. 2011.

[23] Z. Mirzoyan, M. Sollazzo, M. Allocca, A. M. Valenza, D. Grifoni, and P. Bellosta, "Drosophila melanogaster: A Model Organism to Study Cancer," *Frontiers in Genetics*, vol. 10. 2019.

[24] U. B. Pandey and C. D. Nichols, "Human disease models in Drosophila melanogaster and the role of the fly in therapeutic drug discovery," *Pharmacol. Rev.*, vol. 63, no. 2, pp. 411–436, Jun. 2011.

[25] K. Rein, M. Zöckler, M. T. Mader, C. Grübel, and M. Heisenberg, "The Drosophila Standard Brain," *Curr. Biol.*, vol. 12, no. 3, pp. 227–231, Feb. 2002.

[26] J. C. Tuthill, "Lessons from a compartmental model of a Drosophila neuron," *J. Neurosci.*, vol. 29, no. 39, pp. 12033–12034, Sep. 2009.

[27] Y.-H. Tsai, "Millisecond-scale Volumetric Imaging Microscopy for Drosophila Brain Study," 2020.

[28] *Y. Zhou, "Physics 1922 – 1941: Including Presentation Speeches and Laureates' Biographies." Elsevier, 2013.*

[29] R. Homma *et al.*, "Wide-field and two-photon imaging of brain activity with voltage- and calcium-sensitive dyes," *Philos. Trans. R. Soc. Lond. B Biol. Sci.*, vol. 364, no. 1529, pp. 2453–2467, Sep. 2009.

[30] C. Li, L. Gao, Y. Liu, and L. V. Wang, "Optical sectioning by wide-field photobleaching imprinting microscopy," *Appl. Phys. Lett.*, vol. 103, no. 18, p. 183703, Oct. 2013.

[31] J. Pawley, *Handbook of Biological Confocal Microscopy*. Springer Science & Business Media, 2010.

[32] W. Denk, J. H. Strickler, and W. W. Webb, "Two-Photon Laser Scanning Fluorescence Microscopy," *Science*, vol. 248, no. 4951. pp. 73–76, 1990.

[33] G. Sancataldo, L. Silvestri, A. L. A. Mascaro, L. Sacconi, and F. S. Pavone, "Advanced fluorescence microscopy for in vivo imaging of neuronal activity," *Optica*, vol. 6, no. 6. p. 758, 2019.

[34] R. K. P. Benninger and D. W. Piston, "Two-Photon Excitation Microscopy for the Study of Living Cells and Tissues," *Current Protocols in Cell Biology*, vol. 59, no. 1. 2013.

[35] A. H. J. Kim, H. Suleiman, and A. S. Shaw, "New approaches in renal microscopy: volumetric imaging and superresolution microscopy," *Curr. Opin. Nephrol. Hypertens.*, vol. 25, no. 3, pp. 159–167, May 2016.

[36] F. Helmchen and W. Denk, "Deep tissue two-photon microscopy," *Nat. Methods*, vol. 2, no. 12, pp. 932–940, Nov. 2005.

[37] D. A. Benaron *et al.*, "Noninvasive functional imaging of human brain using light," *J. Cereb. Blood Flow Metab.*, vol. 20, no. 3, pp. 469–477, Mar. 2000.

[38] G. Y. Fan, H. Fujisaki, A. Miyawaki, R.-K. Tsay, R. Y. Tsien, and M. H. Ellisman,

"Video-rate scanning two-photon excitation fluorescence microscopy and ratio imaging with cameleons," *Biophys. J.*, vol. 76, no. 5, pp. 2412–2420, May 1999.

[39] K. H. Kim, C. Buehler, and P. T. So, "High-speed, two-photon scanning microscope," *Appl. Opt.*, vol. 38, no. 28, pp. 6004–6009, Oct. 1999.

[40] B. R. Masters, P. T. C. So, and W. W. Mantulin, "Handbook of Biomedical Nonlinear Optical Microscopy," *Journal of Biomedical Optics*, vol. 14, no. 1. p. 019901, 2009.

[41] J. Bewersdorf, R. Pick, and S. W. Hell, "Multifocal multiphoton microscopy," *Opt. Lett.*, vol. 23, no. 9, pp. 655–657, 1998.

[42] Buist, Buist, Muller, Squier, and Brakenhoff, "Real time two-photon absorption microscopy using multi point excitation," *Journal of Microscopy*, vol. 192, no. 2. pp. 217–226, 1998.

[43] V. Nikolenko, B. O. Watson, R. Araya, A. Woodruff, D. S. Peterka, and R. Yuste, "SLM Microscopy: Scanless Two-Photon Imaging and Photostimulation with Spatial Light Modulators," *Front. Neural Circuits*, vol. 2, p. 5, Dec. 2008.

[44] J. P. Parry, R. J. Beck, J. D. Shephard, and D. P. Hand, "Application of a liquid crystal spatial light modulator to laser marking," *Appl. Opt.*, vol. 50, no. 12, pp. 1779–1785, Apr. 2011.

[45] L. Sacconi, E. Froner, R. Antolini, M. R. Taghizadeh, A. Choudhury, and F. S. Pavone, "Multiphoton multifocal microscopy exploiting a diffractive optical element," *Opt. Lett.*, vol. 28, no. 20, pp. 1918–1920, Oct. 2003.

[46] B. O. Watson, V. Nikolenko, R. Araya, D. S. Peterka, A. Woodruff, and R. Yuste, "Two-photon microscopy with diffractive optical elements and spatial light modulators," *Front. Neurosci.*, vol. 4, Sep. 2010.

[47] G. Thériault, Y. De Koninck, and N. McCarthy, "Extended depth of field microscopy

for rapid volumetric two-photon imaging," *Opt. Express*, vol. 21, no. 8, pp. 10095–10104, Apr. 2013.

[48] J. Demas *et al.*, "High-Speed, Cortex-Wide Volumetric Recording of Neuroactivity at Cellular Resolution using Light Beads Microscopy," *bioRxiv*, p. 2021.02.21.432164, Feb. 22, 2021.

[49] R. Lu *et al.*, "Rapid mesoscale volumetric imaging of neural activity with synaptic resolution," *Nat. Methods*, vol. 17, no. 3, pp. 291–294, Mar. 2020.

[50] G. Thériault, M. Cottet, A. Castonguay, N. McCarthy, and Y. De Koninck, "Extended two-photon microscopy in live samples with Bessel beams: steadier focus, faster volume scans, and simpler stereoscopic imaging," *Front. Cell. Neurosci.*, vol. 8, p. 139, May 2014.

[51] T. Chakraborty *et al.*, "Converting lateral scanning into axial focusing to speed up three-dimensional microscopy," *Light Sci Appl*, vol. 9, p. 165, Sep. 2020.
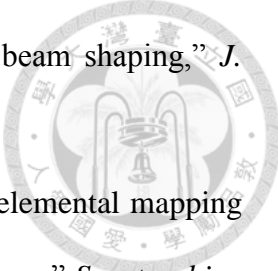
[52] J. Jiang *et al.*, "Fast 3-D temporal focusing microscopy using an electrically tunable lens," *Opt. Express*, vol. 23, no. 19, pp. 24362–24368, Sep. 2015.

[53] M. E. J. Sheffield and D. A. Dombeck, "Calcium transient prevalence across the dendritic arbour predicts place field properties," *Nature*, vol. 517, no. 7533, pp. 200–204, Jan. 2015.

[54] B. N. Ozbay *et al.*, "Three dimensional two-photon brain imaging in freely moving mice using a miniature fiber coupled microscope with active axial-scanning," *Sci. Rep.*, vol. 8, no. 1, p. 8108, May 2018.

[55] L. Kong *et al.*, "Continuous volumetric imaging via an optical phase-locked ultrasound lens," *Nat. Methods*, vol. 12, no. 8, pp. 759–762, Aug. 2015.

[56] S. Piazza, P. Bianchini, C. Sheppard, A. Diaspro, and M. Duocastella, "Enhanced

volumetric imaging in 2-photon microscopy via acoustic lens beam shaping," *J. Biophotonics*, vol. 11, no. 2, Feb. 2018.

[57] He, Chunjing, et al. "Three-dimensional topographic and multi-elemental mapping by unilateral-shift-subtracting confocal controlled LIBS microscopy," *Spectrochim. Acta Part B At. Spectrosc.*, vol. 188, p. 106340, Feb. 2022.

[58] H. Oku, K. Hashimoto, and M. Ishikawa, "Variable-focus lens with 1-kHz bandwidth," *Opt. Express*, vol. 12, no. 10, pp. 2138–2149, May 2004.

[59] M. Göppert-Mayer, "Über Elementarakte mit zwei Quantensprüngen," *Annalen der Physik*, vol. 401, no. 3. pp. 273–294, 1931.

[60] P. T. C. So, "Two-photon Fluorescence Light Microscopy," *eLS*. 2001.

[61] W. R. Zipfel, R. M. Williams, and W. W. Webb, "Nonlinear magic: multiphoton microscopy in the biosciences," *Nat. Biotechnol.*, vol. 21, no. 11, pp. 1369–1377, Nov. 2003.

[62] V. Ntziachristos, "Going deeper than microscopy: the optical imaging frontier in biology," *Nat. Methods*, vol. 7, no. 8, pp. 603–614, Aug. 2010.

[63] E. McLeod and C. B. Arnold, "Optical analysis of time-averaged multiscale Bessel beams generated by a tunable acoustic gradient index of refraction lens," *Appl. Opt.*, vol. 47, no. 20, pp. 3609–3618, Jul. 2008.

[64] K.-J. Hsu, K.-Y. Li, Y.-Y. Lin, A.-S. Chiang, and S.-W. Chu, "Optimizing depth-of-field extension in optical sectioning microscopy techniques using a fast focus-tunable lens," *Opt. Express*, vol. 25, no. 14, pp. 16783–16794, Jul. 2017.

[65] M. Duocastella, B. Sun, and C. B. Arnold, "Simultaneous imaging of multiple focal planes for three-dimensional microscopy using ultra-high-speed adaptive optics," *J. Biomed. Opt.*, vol. 17, no. 5, p. 050505, May 2012.

[66] A. Mermillod-Blondin, E. McLeod, and C. B. Arnold, "High-speed varifocal imaging with a tunable acoustic gradient index of refraction lens," *Opt. Lett.*, vol. 33, no. 18, pp. 2146–2148, Sep. 2008.

[67] T.-W. Chen *et al.*, "Ultrasensitive fluorescent proteins for imaging neuronal activity," *Nature*, vol. 499, no. 7458, pp. 295–300, Jul. 2013.

[68] T. Knöpfel and C. Song, "Optical voltage imaging in neurons: moving from technology development to practical tool," *Nat. Rev. Neurosci.*, vol. 20, no. 12, pp. 719–727, Dec. 2019.

[69] H. Dana *et al.*, "High-performance calcium sensors for imaging activity in neuronal populations and microcompartments," *Nat. Methods*, vol. 16, no. 7, pp. 649–657, Jul. 2019.

[70] H.-Y. Chen, "Enhance Optical Penetration Depth in Drosophila Brain - Minimizing Aberration/scattering from Trachea by Liquid Filling Method," 2022.

[71] J. W. Cha *et al.*, "Reassignment of scattered emission photons in multifocal multiphoton microscopy," *Sci. Rep.*, vol. 4, p. 5153, Jun. 2014.

[72] K. Charan, B. Li, M. Wang, C. P. Lin, and C. Xu, "Fiber-based tunable repetition rate source for deep tissue two-photon fluorescence microscopy," *Biomed. Opt. Express*, vol. 9, no. 5, pp. 2304–2311, May 2018.

[73] J. L. R. Rubenstein and P. Rakic, "Neural Circuit Development and Function in the Healthy and Diseased Brain: Comprehensive Developmental Neuroscience," *Academic Press*, vol. 3, 2013.